nature astronomy

Article

https://doi.org/10.1038/s41550-022-01875-w

An Ice Age JWST inventory of dense molecular cloud ices

Received: 3 October 2022

Accepted: 1 December 2022

Published online: 23 January 2023

Check for updates

M. K. McClure[1] ✉, W. R. M. Rocha[2], K. M. Pontoppidan[3], N. Crouzet[1], L. E. U. Chu[4], E. Dartois[5], T. Lamberts[1,6], J. A. Noble[7], Y. J. Pendleton[8], G. Perotti[9], D. Qasim[10], M. G. Rachid[2], Z. L. Smith[11], Fengwu Sun[12], Tracy L. Beck[3], A. C. A. Boogert[13], W. A. Brown[14], P. Caselli[15], S. B. Charnley[16], Herma M. Cuppen[17], H. Dickinson[11], M. N. Drozdovskaya[18], E. Egami[12], J. Erkal[13], H. Fraser[11], R. T. Garrod[19], D. Harsono[20], S. Ioppolo[21], I. Jiménez-Serra[22], M. Jin[16,23], J. K. Jørgensen[24], L. E. Kristensen[24], D. C. Lis[25], M. R. S. McCoustra[26], Brett A. McGuire[27,28], G. J. Melnick[29], Karin I. Öberg[29], M. E. Palumbo[30], T. Shimonishi[31], J. A. Sturm[1], E. F. van Dishoeck[1] & H. Linnartz[2]

Icy grain mantles are the main reservoir of the volatile elements that link chemical processes in dark, interstellar clouds with the formation of planets and the composition of their atmospheres. The initial ice composition is set in the cold, dense parts of molecular clouds, before the onset of star formation. With the exquisite sensitivity of the James Webb Space Telescope, this critical stage of ice evolution is now accessible for detailed study. Here we show initial results of the Early Release Science programme Ice Age that reveal the rich composition of these dense cloud ices. Weak ice features, including $^{13}CO_2$, OCN^-, ^{13}CO, OCS and complex organic molecule functional groups, are now detected along two pre-stellar lines of sight. The $^{12}CO_2$ ice profile indicates modest growth of the icy grains. Column densities of the major and minor ice species indicate that ices contribute between 2% and 19% of the bulk budgets of the key C, O, N and S elements. Our results suggest that the formation of simple and complex molecules could begin early in a water-ice-rich environment.

In molecular clouds, the volatile elements that make up life as we know it (carbon, hydrogen, oxygen, nitrogen and sulfur, that is CHONS) are locked up in ices on the surfaces of dust grains. The vibrational modes of these molecular ices are observed in absorption against the near- and mid-infrared continuum provided by field stars located behind clouds. Fully resolved absorption bands have logarithmic depths directly proportional to the ice column density along the line of sight, allowing model-independent assessment of relative ice abundances within the same beam. At low extinctions in the outer regions of clouds, a mixture of water (H_2O), methane (CH_4) and ammonia (NH_3) ice forms initially through accretion of atomic H in combination with atomic O (refs. [1,2]), C (refs. [3,4]) and N (refs. [5,6]) onto silicate/carbon-rich dust grains. Carbon dioxide (CO_2) also forms efficiently in this water-ice layer. In the densest and coldest cloud cores, carbon monoxide (CO) freeze-out forms a CO-dominated ice phase[7,8], where CO_2 and other simple ice species continue to form. CO and its reaction products can be hydrogenated to produce methanol (CH_3OH)[9] or have a hydrogen atom abstracted[10], and subsequent radical–radical reactions can also lead to the formation of other complex organic molecules (COMs). These simple ices and methanol should provide the feedstock for more complex COMs, such as the biomolecule glycine that is seen in comets[11], some of which are also capable of forming under pre-stellar core conditions[12]. Ground-based telescopes and space observatories, such as the Infrared Space Observatory[13], Spitzer[14] and Akari[15], have probed ice

A full list of affiliations appears at the end of the paper. ✉e-mail: mcclure@strw.leidenuniv.nl

https://doi.org/10.1038/s41550-022-01875-w

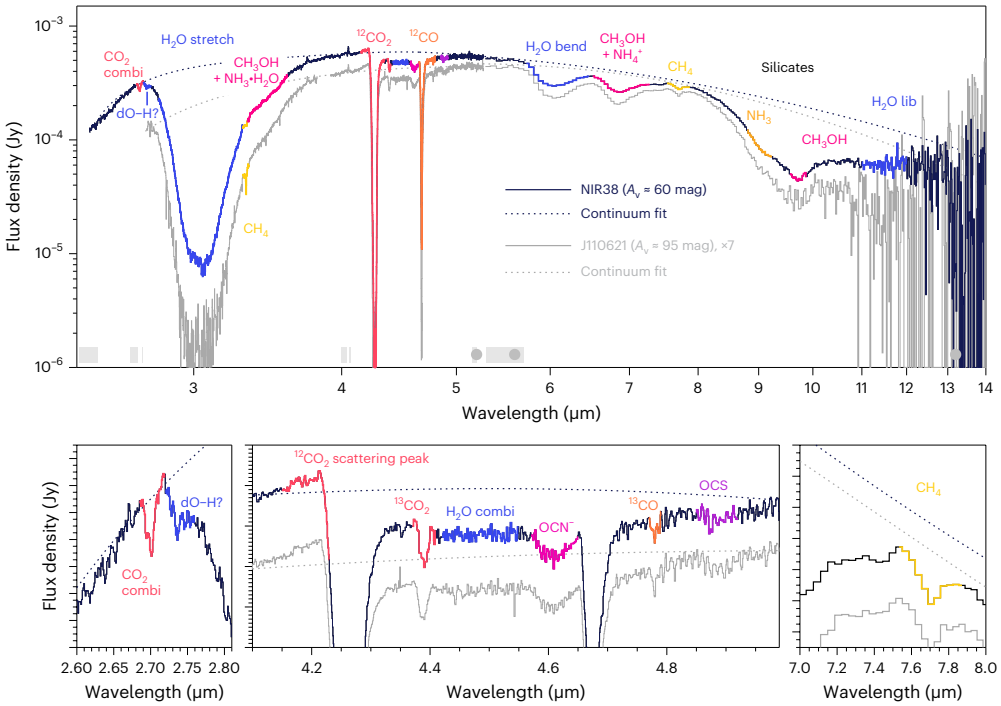

Fig. 1 | NIRSpec FS (NIRCam WFSS) and MIRI LRS spectra of NIR38 and J110621. Top: full NIRSpec FS and MIRI LRS spectra of NIR38 ($A_V \approx 60$ mag, solid navy line) and J110621 ($A_V \approx 95$ mag, solid light grey line), with associated continuum fits (dotted lines). For NIR38, a preliminary NIRCam WFSS spectrum has been scaled to the NIRSpec spectrum at 3.8 μm and spliced in to cover the NIRSpec FS gap from 3.85 μm to 3.9 μm and extend the spectrum to 2.5 μm. Ice absorption features are colour-coded according to species and labelled in the NIR38 spectrum. Wavelength regions used for the continuum fit are indicated by light grey bars (NIRSpec) and dark grey filled circles (MIRI) at the bottom of the top panel. Bottom: zoom-in on the weaker ice features and structure revealed by JWST. The potential dangling O–H feature is indicated by 'dO–H', the combination modes of CO_2 and H_2O by 'combi', and the libration mode of H_2O by 'lib'.

chemical evolution along sightlines through the envelopes of nascent protostars. However, chemical assays of cloud ice have been limited to regions with visual extinctions below $A_V \approx 50$ mag, due to the faintness of field stars seen at larger A_V (refs. [16,17]).

Here we report initial observations of pristine cloud ices at $A_V > 50$ mag towards two background stars, NIR38 (11:06:25.39, −77:23:15.70, J2000) and SSTSL2J110621.63-772354.1 (hereafter J110621; 11:06:21.70, −77:23:53.50, J2000), using the James Webb Space Telescope (JWST). These stars probe dense lines of sight just outside the infalling envelope of a class 0 protostar, Cha MMS1 (ref. [18]) in the low-mass star-forming region Chameleon I (192 pc (ref. [19])). Initial calculations of their extinction based on the intrinsic colours of K and G giant stars and mid-infrared photometry suggest values of $A_V \approx 60$ mag and $A_V \approx 95$ mag, respectively (see section 3.4 in ref. [20]), or hydrogen column density $N_H = 1.1 \times 10^{23}$ cm^{-2} and $N_H = 1.7 \times 10^{23}$ cm^{-2}, respectively. The JWST observations presented here were obtained with the Near Infrared Spectrograph (NIRSpec)[21] Fixed Slit (FS) mode ($R \approx 2{,}600$, 2.7–5.3 μm), the Near Infrared Camera (NIRCam)[22] Wide Field Slitless Spectrograph (WFSS) mode ($R \approx 1{,}600$, 2.4–5.0 μm) and the Mid-Infrared Instrument (MIRI)[23] Low Resolution Spectrograph (LRS) FS mode ($R \approx 100$, 5–14 μm) (see Methods for more details), to cover all five major simple ice species, H_2O, CO_2, CO, CH_4 and NH_3, and the simplest COM, CH_3OH.

The full, multi-instrument 2.5–14 μm spectra towards both high-A_V background stars are presented in the top panel of Fig. 1, with major solid-state features labelled. The identifications of features that we detect, tentatively detect and do not detect are presented in Table 1. The spectra obtained from each instrument are compared in Fig. 2; NIR38 is detected in the continuum at 3.97 μm by NIRSpec FS with 547.1 ± 2.6 μJy (signal-to-noise, S/N, ≈ 207) and NIRCam WFSS with 551.2 μJy, while its flux at 7.5 μm with MIRI LRS is 310.7 ± 0.6 μJy (S/N ≈ 499). J110621 was detected at 3.97 μm by NIRSpec FS with 54.4 ± 0.4 μJy (S/N ≈ 145) and by MIRI LRS at 7.5 μm with a flux of 39.7 ± 0.2 μJy (S/N ≈ 208). This high sensitivity allows us to detect both the expected strong absorption features of abundant ice species and a number of weak absorption features that are now detectable through quiescent molecular cloud lines of sight (Fig. 1, bottom, and Fig. 3). For these spectra, we fit a global continuum to specific continuum regions (Methods and Fig. 1 caption) to calculate optical depths for these ices.

We report column densities and abundances relative to water of the different ice species in Fig. 4 and Table 2, as determined from both global and local fitting of laboratory data (Table 3) to the optical depths over the whole wavelength range (see Methods and fits given by Extended Data Figs. 1–3) and to individual ice features (Supplementary Figs. 1 and 2). We also consider the shape of the ice bands, which depends on the local environment, in particular whether the ice is mixed with water or not.

Results

Ice inventory and new features

Both spectra in Fig. 1 display all of the deep features that we expect to be associated with the main icy grain constituents: H_2O ice, the main isotopologue of both major C-bearing ices, $^{12}CO_2$ and ^{12}CO, and rocky silicates. The column density of water ice increases from $N_{H2O} \approx 7 \times 10^{18}$ cm^{-2} to $N_{H2O} \approx 13 \times 10^{18}$ cm^{-2}, respectively, between NIR38 and J110621, while CO_2 and CO are present at 10–20% and 20–40% of H_2O ice. In addition, the sensitivity and spectral resolution of NIRSpec also allow us to detect a number of new features that probe the structure of these main ices, as well as the chemical diversity of additional small molecules in the ice.

Inorganic O and C ices. In these simple ice species, we see structure in the $^{12}CO_2$ stretching feature at 4.27 μm, with both an excess emission over the continuum in the blue wing at 4.2 μm and a strong absorbing red wing that extends to at least 4.35 μm. While the continuum shape may change slightly with future photospheric model fits, there

https://doi.org/10.1038/s41550-022-01875-w

Table 1 | Absorption features of molecules in ices and dust features observed towards NIR38 ($A_V \approx 60$ mag) and J110621 ($A_V \approx 95$ mag)

λ (μm)	ν (cm^{-1})	Species	Identification	Detection	
				NIR38	J110621
2.69	3,708	CO_2	Combination	✓	–
2.73	3,664	H_2O	O–H dangling bond	✓	–
3.0	3,330	H_2O	O–H stretch	✓	✓
3.24	3,249	CH_3OH	O–H stretch	✓	✓
3.32	3,012	CH_4	C–H stretch	✓	✓
3.47	2,881	$NH_3{\cdot}H_2O$	N–H stretch	!	!
3.32–3.64	3,012–2,890	CH_3OH	C–H asymmetric stretch + overtone	✓	✓
3.92	2,548	H_2S	S–H	✗	–
4.07	2,457	HDO	O–D stretch	✗	✗
4.17–4.77	2,400–2,100	H_2O	Combination	✓	✓
4.27	2,340	$^{12}CO_2$	C–O stretch	✓	✓
4.38	2,280	$^{13}CO_2$	C–O stretch	✓	✓
4.44	2,252	CH_3CN	C–N stretch	✗	✗
4.59	2,175	OCN^-	C–N stretch	✓	✓
4.67	2,140	^{12}CO	C–O stretch	✓	✓
4.76	2,100	HCN	C≡N stretch	✗	✗
4.78	2,090	^{13}CO	C–O stretch	✓	✓
4.90	2,040	OCS	C–O stretch	✓	✓
6.0	1,666	H_2O	Bending	✓	✓
6.85	1,459	CH_3OH	CH_3 deformation	✓	✓
6.85	1,459	NH_4^+	N–H stretch	✓	✓
6.9–7.5	1,449–1,333	Unidentified absorption	COMs functional groups?	✓	✓
7.24	1,384	CH_3CH_2OH?	CH_3 deformation	!	!
7.43	1,362	CH_3CHO?	CH_3 def. + CH wagging	!	!
7.60	1,318	SO_2	S–O stretch	!	!
7.71	1,300	CH_4	C–H stretch	✓	✓
8.86	1,131	CH_3OH	CH_3 rock	✓	✓
9.01	1,110	NH_3	Umbrella	✓	✓
9.74	1,025	CH_3OH	C–O stretch	✓	✓
9.80	1,020	Silicate	Si–O stretch	✓	✓
11.0	910	H_2O	Libration wing	✓	✓

Symbol legend: ✓, observed; ✗, not observed; !, possibly observed, –, insufficient data.

is no physically motivated fit that could locally change the continuum enough to erase the warped profile. A similar asymmetric profile is theoretically expected to result from ice mantle growth[24]. An analogous scattering profile is tentatively seen in the CO band at 4.7 μm, where there is redshifted absorption below the continuum. However, the blueshifted CO excess requires confirmation, as it overlaps other absorption features. We also detect both the combination mode of $^{12}CO_2$ at 2.7 μm and perhaps the dangling O–H mode of H_2O at 2.74 μm (Extended Data Fig. 1b, inset), the latter of which would signify that some fraction of the water ice is porous or interacting with a mixture of other species. The ^{13}C isotopologues of CO_2 and CO are both detected (Extended Data Figs. 4 and 5, respectively), superimposed over the 4.6–5.0 μm CO ro-vibrational gas-phase lines originating in the stellar photospheres of these background stars. The $^{12}CO_2/^{13}CO_2$ ratio ranges from 69 to 87 towards these two lines of sight, while the $^{12}CO/^{13}CO$ ratio ranges from 99 to 169.

N-rich ices. We detect the main N-carrying ice, NH_3, in isolation at 9.1 μm after the removal of the broad 10 μm silicate feature profile from the optical depth spectrum (Extended Data Fig. 6), along with a blended ammonium (NH_4^+) feature at 6.85 μm, which have both been seen before towards dense cores. However, with JWST we are now able to detect the cyanate anion (OCN^-) at 4.62 μm, where it overlaps with the blue scattering wing of ^{12}CO (Extended Data Fig. 7). Ammonium (NH_4^+), a potential counter ion, is also detected, securing the identification of OCN^-. In contrast, we do not detect other small nitriles, such as CN, HCN and CH_3CN (Methods). The upper limits to these ice column densities range from 0.7% to 2% of H_2O in our spectra. This limit is similar to the 0.1–1% level of HCN seen in comets[25].

S-rich ices. In these spectra, we detect the S-bearing ice species carbonyl sulfide (OCS) around 4.9 μm, superimposed on the stellar photospheric CO absorption features (Extended Data Fig. 8).

https://doi.org/10.1038/s41550-022-01875-w

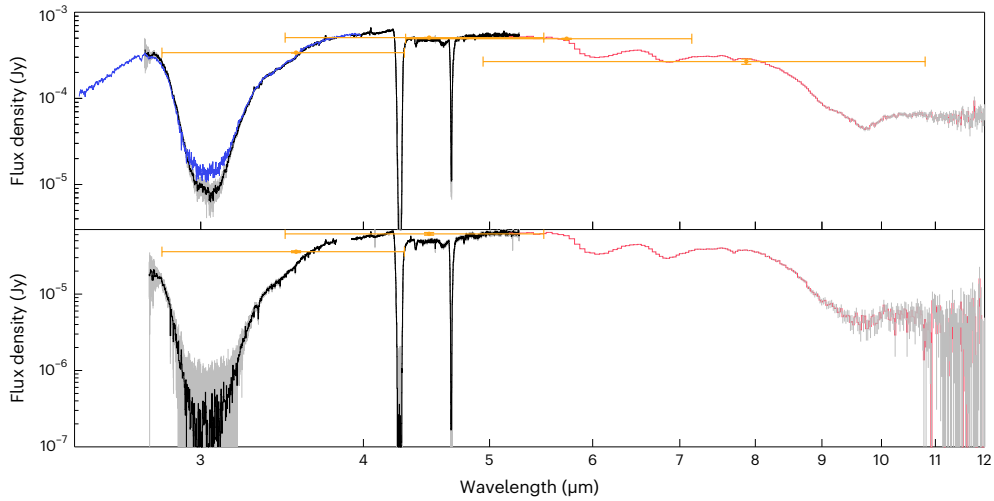

Fig. 2 | Data quality comparison for NIR38 and J110621. Top: comparison of the NIRCam WFSS (blue), NIRSpec FS (black) and MIRI LRS FS (red) spectra of the $A_V = 60$ mag background star. Error bars (grey) are 3σ, and in some regions are smaller than the thickness of the lines. Spitzer IRAC photometry (gold points) from the IPAC SEIP catalogue is given for reference, with error bars and bandpass indicated. Bottom: comparison of NIRSpec FS and MIRI LRS FS data for the $A_V = 95$ mag star. Colours are the same as in the top panel.

The simultaneous detection of OCS and CO ice is consistent with a solid-state formation mechanism of CO + S → OCS (ref. [26]), but constraining the intimate chemical environment of OCS would require careful removal of the photospheric features. There are hints of another S-bearing ice, SO_2, at 7.6 μm in the blue shoulder of the CH_4 feature, with detection limits of 0.1–0.3% with respect to water. The source of sulfur for OCS and potentially SO_2 could be from gas-phase depletion into the ice[27], as well as from minerals, such as troilite (FeS)[28]. However, the dominant S-bearing ice in comets, hydrogen sulfide (H_2S)[29], remains undetected at an upper limit of 0.6% of H_2O, as the 3.92 μm feature is not detected towards NIR38. This limit is comparable to the 1% level of H_2S seen in comets[25].

Organic ices. We detect both bands of the simple organic ice CH_4, at 3.32 μm and 7.6 μm. Another low-contrast feature appears from 3.35–3.6 μm in the red wing of the water-ice band. This feature has been detected before towards background stars, but we detect it here with an S/N of 150 and 70 in the $A_V = 60$ mag and $A_V = 95$ mag sources, respectively. At this sensitivity, the feature separates into four distinct peaks that are reproducible between the NIR38 NIRCam and NIRSpec spectra, as well as between NIR38 and J110621 (Methods). These features are consistent with a blend between the C–H stretch of CH_3OH and a broad component centred at 3.47 μm (Extended Data Fig. 9). Ammonia hydrates ($NH_3{\cdot}H_2O$) are considered to be the primary contender for this broad component[30], but the sensitivity of our observations will enable a differential diagnosis in a future work. As seen in previous dense cloud spectra, methanol ice is detected additionally in isolation at 9.7 μm and blended with the NH_4^+ feature at 6.85 μm. There is excellent agreement between the column densities derived from both methanol features (Supplementary Fig. 2). Although the 6 μm and 6.85 μm features appear smooth at $R \approx 100$ in both sources, there are weak but robust absorption excesses at 6.94 μm, 7.06 μm, 7.24 μm and 7.43 μm (Fig. 3) attributable to the functional group in COMs caused by the asymmetric deformation mode of CH_3 (ref. [31]), which has been tentatively detected with Spitzer[14] and JWST[32]. These two bands are seen in the infrared spectra of acetone (CH_3COCH_3)[33], ethanol (CH_3CH_2OH)[31] and acetaldehyde (CH_3CHO)[31]. These background stars will require the higher spectral resolution of MIRI MRS to confirm these identifications, and determine the COM chemical environment and the degree to which complex chemistry has begun along the J110621 sightline.

Stable ice chemical environment from $A_V \approx 20$ mag to $A_V \approx 95$ mag

The absolute column densities of most ice species are slightly larger towards J110621, as expected from the increase to $A_V \approx 95$ mag. However, the ice inventory is very similar towards both sightlines, suggesting that although the total amount of ice increases, the ice composition is set at a lower A_V. In fact, the relative column densities of the simple ices from 60 mag < A_V < 95 mag are broadly consistent with the ice evolution sequence proposed on the basis of Spitzer observations from 20 mag < A_V < 50 mag (ref. [16]), as exemplified by the comparison with the background star Elias 16 ($A_V \approx 19$ mag) in Fig. 4 as well as laboratory data and chemical modelling of this dense cloud region[20]. These results suggest that although CO ice is the second most abundant species detected in our spectra, the local cloud gas hydrogen number density, n_H, may be less than the limit of $n_H \approx 10^5$ cm^{-3} required for CO to catastrophically freeze-out via collisions[7,8]. Supporting this, initial modelling of the ^{12}CO-ice profiles (Extended Data Figs. 1 and 2) suggests that they may be dominated by a pure component, with two additional weaker components mixed with methanol or CO_2 (ref. [16]). In contrast, the local $^{13}CO_2$ ice profiles of both stars suggest that CO_2 is dominated by an intimate mixture with H_2O, with a lesser contribution from a CO-rich mixture (Methods and Extended Data Fig. 4). In addition, based on comparisons between laboratory data and the profiles of the ^{12}CO and 9.7 μm methanol bands, methanol seems to reside in environments containing both H_2O and CO (Methods and Extended Data Figs. 1 and 2). The amount of methanol appears to be approximately the same in both sources, based on both the 3.53 μm and 9.7 μm features. In contrast, there are constant or increasing column densities of the simple hydrides, NH_3 and CH_4.

Discussion

The sum of the column densities for both CO isotopologue ices and their potential reaction products is less than the expected total CO column density from A_V for each line of sight, suggesting that at most 46% and 33% of the available CO gas has frozen out into ices towards NIR38 and J110621, respectively. Although NIR38 samples a smaller total column of dust, its line of sight appears to pass closer to the class 0 protostar (Extended Data Fig. 10). If this region contains locally denser or colder dust, it could explain the larger fraction of total CO that is frozen out onto the grains. These results imply that the rich variety of ices

https://doi.org/10.1038/s41550-022-01875-w

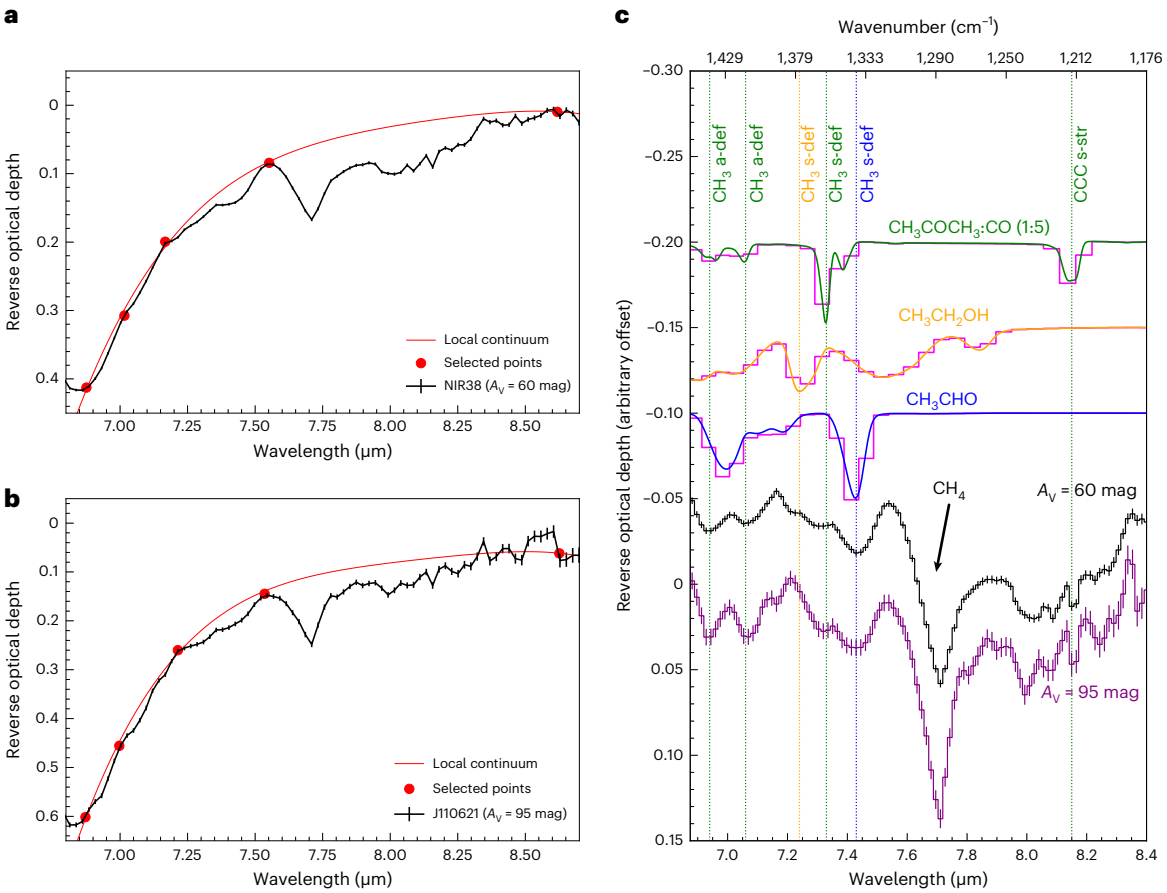

Fig. 3 | Detections of COM functional groups. a,**b**, Local continuum over the optical depth spectra of NIR38 (A_V = 60 mag; **a**) and J110621 (A_V = 95 mag; **b**) in the range between 6.9 μm and 8.6 μm. **c**, Local continuum subtracted spectra of NIR38 (A_V = 60 mag) and J110621 (A_V = 95 mag) compared with laboratory infrared spectrum of COMs (CH_3CHO, green line[31]; CH_3CH_2OH, orange line[31]; CH_3COCH_3:CO, blue line[33]) in the solid phase. The magenta line shows the laboratory spectra degraded to a resolving power of 150. The vertical lines indicate the match of the experimental data with the observations. The asymmetric deformation (a-def), symmetric deformation (s-def) and symmetric stretching (s-str) vibrational modes of the experimental data are indicated.

that we see probably formed early, before catastrophic CO freeze-out, rather than later through purely CO hydrogenation pathways.

The other ice column density results are also consistent with efficient, early formation of CO_2, NH_3 and CH_4 in water-rich ices through H addition and abstraction[3,6,34,35], followed by a small amount of the subsequent CO-based chemistry that we would expect to see at these high extinctions. While methanol was traditionally thought to form efficiently via successive CO hydrogenation, with H_2CO as an intermediate[9], it can also form earlier and more slowly in the H_2O-rich ice phase[36,37]. Our fit to the feature at 9.7 μm suggests that both formation pathways may operate in these ices. This conclusion is supported by the detection of functional groups of COMs at 7–7.5 μm towards pre-stellar sources that lie outside of the coldest cores in this region, suggesting their early formation in the water-rich phase[10]. Models predict only ethanol at $N \approx 6 \times 10^{16}$–$15 \times 10^{16}$ cm^{-2} (ref. [20]), which is broadly consistent with the optical depths at 7.2 μm in both spectra, but not the other potential COM species that could produce the other absorption features seen at 6.94 μm, 7.06 μm and 7.34 μm. Our detections of COM functional groups in these pre-stellar ices hint at the non-energetic complexity achieved in ices already before the formation of a hot protostellar core.

Accounting for the amount of C, O, N and S in the ices is critical to determine the bulk volatile budget of the stellar and planetary systems that will form within this molecular cloud. Comparing the column densities of the detected ices for both NIR38 and J110621 with the expected cosmic abundances for C, O, N and S, we see at most 19% of the total O and C budgets, 13% of the total N budget, and 1% of the S budget in this dense cloud (Methods). These numbers are similar to what has been previously reported for protostars[16], but now we are able to trace the budgets of these elements back to their initial conditions in dense clouds. Most of the remaining budgets will be made up of refractory species, including silicates and amorphous carbons, or other ices such as N_2 that do not show spectral features at these wavelengths. Some of the budget may additionally be accounted for in COMs that we cannot yet identify conclusively with the MIRI LRS spectral resolution.

The profile distortions of the deepest ice bands show that the increase in H_2O, CO_2 and CO is accompanied by an increase in the size of these icy grains. The enhanced, redshifted absorption wing, as seen in H_2O and CO_2 (for example, ref. [38]), in addition to the blueshifted emission wing described earlier for the $^{12}CO_2$ and possibly ^{12}CO-ice features[24], are associated with scattering effects resulting from icy grain growth to sizes on the order of the wavevector at which they are detected, that is, a few micrometres. Whereas red wing extinction due to scattering is a rather robust effect produced by larger grains, the intensity of the blue emission excess can be highly variable. Its strength is highly sensitive to specific local changes in the optical constants of the grains' core and mantle materials. The profiles of our observed CO_2 ice features imply growth to sizes of around 1 μm, as predicted by some grain growth models (for example, refs. [39,40]). Despite this relatively modest increase in maximum grain size, the observed growth occurs at the expense of the smaller grains, which are depleted. Our observed

https://doi.org/10.1038/s41550-022-01875-w

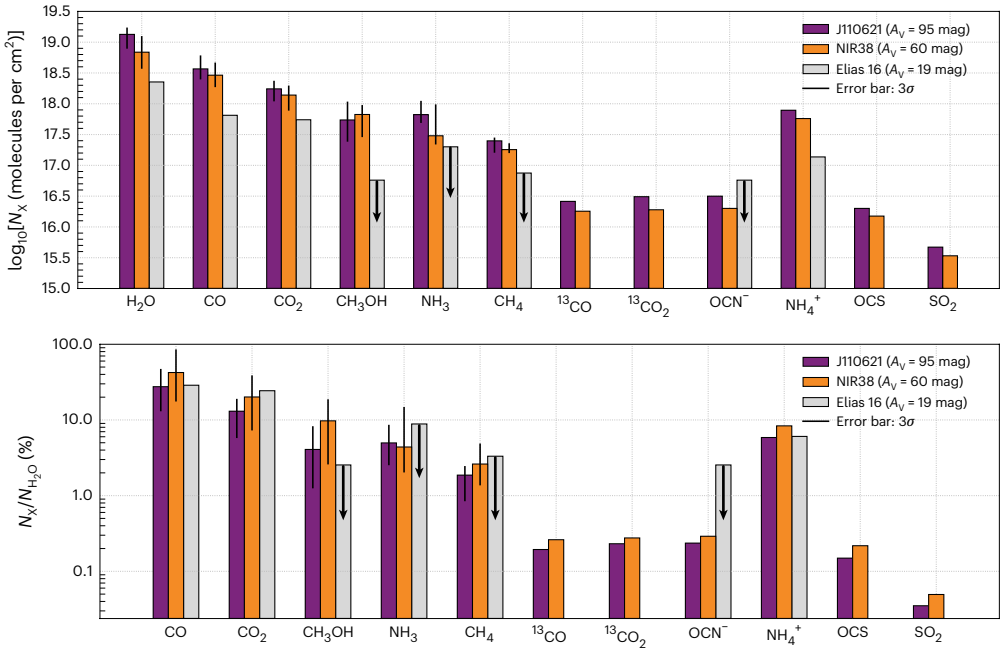

Fig. 4 | Derived ice column density for different species towards NIR38 ($A_V \approx 60$ mag) and J110621 ($A_V \approx 95$ mag). Top: column densities of the ice species identified in this work, compared with the literature values of Elias 16 ($A_V \approx 19$ mag)[55]. The column densities of the major ice components are from the global ENIIGMA fit (best of $n = 112$ models), and we use the values from the local fits for the minor ice components. Black arrows indicate upper limits and error bars are taken from the 3σ confidence intervals. Bottom: relative column densities of the detected ices, normalized to H_2O ice. Black arrows indicate upper limits and error bars are taken from the 3σ confidence intervals.

change in icy dust grain size distribution would not only influence the visual extinction but also reduce the total grain surface available for reactions in such dense regions. However, our tentative detection of the OH dangling mode of H_2O near 2.7 μm could suggest that the water in these large grains is porous or mixed with other ices. In that event, the pore surfaces may also provide space for additional reactions.

Detailed modelling to quantify the maximum grain size, shape and porosity of these ices will be presented in a future work. Further analysis of the reaction pathways and relative ice abundances requires both chemical modelling and future observations of molecular clouds at both low and high A_V values to confirm when the simple hydrides are formed in relation to CO freeze-out. Complementary molecular gas-phase observations will also confirm the extent to which CO has frozen out in this region. Such work will in part continue through another component of the Ice Age Early Release Science programme, in which we have obtained hundreds of ice spectra in the same Chameleon I region with the new multi-object capabilities of NIRCam WFSS. By combining these datasets, the superlative sensitivity, spectral resolution and wavelength coverage with JWST now enable us to fully probe the initial conditions of all of the major ices in molecular cloud cores just before their collapse to form protostars. These new capabilities open the door to understanding the formation and inheritance of these key CHONS species through the star- and planet-formation process and, ultimately, address what role they will play in shaping the chemistry on emerging planets.

Methods

Observations and data reduction

NIRSpec. NIRSpec FS[21] observations of the targets NIR38 ($A_V = 60$ mag) and SSTSL2J110621.63-772354.1 ($A_V = 95$ mag) were taken on 6 July 2022 and 8 July 2022, respectively, using the G395H grating, combined with F290LP blocking filter. Target acquisition was achieved using the Wide Aperture Target Acquisition method and the SUB2048 subarray with the CLEAR filter and a readout pattern of NRSRAPID6 with an exposure time of 14.5 s for both sources. Spectra of the two stars were obtained using the ALLSLITS subarray at four dither positions, spaced along the S200A2 slit. Each integration was composed of 57 groups and 265 groups using the NRSRAPID readout pattern, for total on-source exposure times of 1,274.7 s. and 5,845.7 s, respectively.

The JWST calibration pipeline was used for detector level 1 processing to calculate rate files from the uncalibrated ramps using version 1.7.1, Calibration Reference Data System (CRDS) context jwst_0948.pmap, and the public PUB CRDS server. The two-dimensional rate spectra were distortion corrected using a second-order trace function derived from a commissioning observation of the standard star TYC 4433-1800-1, observed as part of programme PID 1128. The two-dimensional spectral dithers were pairwise differenced to efficiently remove the background, and a one-dimensional spectrum from each dither was then optimally extracted[41] using a cross-dispersion profile calculated by median-collapsing each dither in the spectral direction. An uncalibrated spectrum was then derived using a median for the four separate dithers to remove most cosmic rays. Note that the observation of SSTSL2J110621.63-772354.1 used very long integrations (>1,000 s), and suffers from large numbers of cosmic ray hits, not all of which could be fully corrected. To flux calibrate the spectra, we extracted spectra from the identically processed level 1 rate files of the standard star observation of TYC 4433-1800-1 using the same grating and slit. By dividing with the standard star spectrum, and multiplying by a model spectrum of the standard star, scaled to $K_S = 11.584$ mag, we arrive at the final, calibrated spectra. This yielded excellent results, although the direct use of the standard star leave a small number of artefacts from uncorrected hydrogen absorption lines in the standard star spectrum. Note that this process does not rely on pipeline flat fields or calibrations, which are not yet available. However, the wavelength calibration does use the solution from the pipeline. Errors were formally propagated from pixel errors estimated by the ramps-to-slopes fits from the level 1 processing.

https://doi.org/10.1038/s41550-022-01875-w

Table 2 | Integrated optical depths and column densities of molecules in ices observed towards NIR38 ($A_V \approx 60$ mag) and J110621 ($A_V \approx 95$ mag)

Species	ν (cm^{-1})	A (cm per molecule)	$\int \tau_\nu d\nu$[a]		N_{ice} ($\times 10^{18}$ cm^{-2})[b]	
			NIR38	J110621	NIR38	J110621
H_2O	3,330	2×10^{-16} (ref. [59])	1,376.07	2,676.12	$6.88^{12.5}_{3.70}$ (6.93)	$13.38^{17.27}_{7.83}$ (13.17)
^{12}CO	2,140	1.1×10^{-17} (ref. [59])	32.56	40.48	$2.96^{4.66}_{1.86}$ (3.22)	$3.68^{5.46}_{2.48}$ (3.94)
^{13}CO	2,090	1.0×10^{-17} (ref. [59])	0.32	0.31	$0.03^{0.04}_{0.02}$ (0.02)	$0.02^{0.03}_{0.01}$ (0.02)
$^{12}CO_2$	2,340	1.1×10^{-16} (ref. [59])	151.8	191.4	$1.38^{1.97}_{0.77}$ (1.36)	$1.74^{2.36}_{1.09}$ (1.62)
$^{13}CO_2$	2,280	7.1×10^{-17} (ref. [59])	1.42	2.30	$0.02^{0.03}_{0.01}$ (0.03)	$0.02^{0.04}_{0.02}$ (0.03)
CH_3OH[c]	2,830	1.3×10^{-16} (ref. [57])	53.3 {68.9}	58.5 {84.5}	0.41 {0.53}	0.45 {0.65}
CH_3OH	1,025	1.8×10^{-17} (ref. [76])	10.98	9.18	$0.61^{0.95}_{0.28}$ (0.54)	$0.51^{1.08}_{0.24}$ (0.49)
NH_3	1,110	2.1×10^{-17} (ref. [76])	6.31	13.86	$0.30^{0.97}_{0.21}$ (0.41)	$0.66^{1.11}_{0.48}$ (0.68)
CH_4	1,303	8.4×10^{-18} (ref. [76])	1.51	2.11	$0.18^{0.23}_{0.14}$ (0.16)	$0.25^{0.28}_{0.16}$ (0.28)
OCN^-	2,175	1.3×10^{-16} (ref. [64])	2.58[d]	4.11[d]	0.02	0.03
NH_4^+	1,459	4.4×10^{-17} (ref. [77])	25.08[d]	34.32[d]	0.57	0.78
OCS	2,040	1.2×10^{-16} (ref. [69])	1.18[d]	2.36[d]	0.01	0.02
SO_2	1,310	3.4×10^{-17} (ref. [78])	0.11[d]	0.16[d]	0.0034	0.0047
			1σ upper limits			
H_2S	2,548	1.7×10^{-17} (ref. [69])	0.64[e]	–	0.04	–
HCN	2,100	1.0×10^{-17} (ref. [71])	0.66[e]	0.88[e]	0.06	0.09
CH_3CN	2,252	1.9×10^{-18} (ref. [70])	0.26[e]	0.35[e]	0.14	0.19

[a]When not indicated, these values are based on the global fit. [b]Upper and lower values are from 3σ confidence intervals. Values inside the parenthesis are calculated from local fits. See Supplementary Information. [c]Calculations performed on optical depth data after local continuum extraction around 3.5 μm. See Extended Data Fig. 9. Values inside the curly brackets are obtained excluding the ammonia hydrate effect. [d]Values from the local fits. See Supplementary Information. [e]$\int \tau_\nu d\nu$=RMS×FWHM.

NIRCam. NIRCam WFSS[22] grism observations of the Cha-MMS 1 field were taken on 3 July 2022 with the F322W2 filter (2.5–4.0 μm) using Grism C with NIR38 (A_V = 60 mag) residing in module A. We obtained 24 individual integrations of the field with a total exposure time of 1.7 h. We followed a data reduction routine similar to that in ref. [42]. We first reduced the grism spectroscopic data with the standard JWST calibration pipeline v1.6.2 to the level of Stage 1, using the default CRDS set-up with JWST's operational pipeline, OPS, and no modifications, that is CRDS context 0953, and then performed two-dimensional sky-background subtraction using the sigma-clipped median images that were constructed from the obtained WFSS data. Flat-field correction was also applied using the imaging flat data obtained with the same filter. We then extracted the spectra of the two background stars using the optimal extraction method[41] from each individual integration, and co-added them together using the SpectRes package[43]. The wavelength and flux calibrations were performed using the in-flight measurements obtained with JWST Commissioning Program #1076. At this stage, it is important to note that the current background subtraction method has not been fully optimized, so small systematic offsets may exist within data. In addition, the optimal extraction method reduces, but may not entirely eliminate, potential flux contamination from other nearby sources. Therefore, we may be marginally overestimating the flux for our A_V = 60 mag source.

MIRI LRS. MIRI LRS FS[23] observations of the targets NIR38 (A_V = 60 mag) and SSTSL2J110621.63-772354.1 (A_V = 95 mag) were taken on 4 July 2022 and 11 July 2022, respectively. Target acquisition was achieved using the F560W filter with a FAST readout pattern with 4 groups per integration for an exposure time of 11.1 s for both sources. These two targets used observations with 40 groups per integration and 104 groups per integration, respectively, with 5 integrations per exposure with a two-nod dither pattern along the slit, for a total of 10 total integrations per source and total exposure times of 1,132.2 s and 2,908.2 s, respectively. The FASTR1 readout pattern was used.

We reduced the data with the same procedure for the two sources. We used the STScI JWST pipeline (https://jwst-pipeline.readthedocs.io) version 1.8.2, the PUB CRDS server, and CRDS context jwst_0986.pmap to obtain the Stage 1 and Stage 2 products. We started from the uncalibrated data (Level1b, 'uncal' files). We ran the Detector1Pipeline with default parameters and the Spec2Pipeline step by step. We used each dither position as a background image for the other and subtracted the background pixel-wise. From the calibrated images ('cal' files), we extracted a one-dimensional spectrum from each dither position using the optimal extraction method[41] where a cross-dispersion profile is calculated by median-collapsing the two-dimensional spectral trace in the spectral direction. The spectra from both dither positions were averaged to obtain a final spectrum. As a comparison, we extracted a spectrum using the JWST Spec3Pipeline. We combined the two dither positions into a single image using the 'resample_spec' step and extracted the one-dimensional spectrum using the 'extract_1d' step. We defined the extraction region in a custom reference file and disabled the offset that accounts for the expected location of the source ('use_source_posn' set to 'False'). This ensured that the aperture was centred on the source. We also extracted spectra from the 'cal' files using a simple aperture method (not relying on 'extract_1d') and from the resampled image using the optimal extraction method. All these spectra are in good agreement but the optimal extraction method applied on the 'cal' files provides a smoother spectrum, which we kept for scientific interpretation. The CRDS context jwst_0986.pmap uses a wavelength calibration that has been updated for MIRI LRS FS after an initial mismatch that was found between the flight calibration and the first extracted science spectra. This new wavelength calibration (encoded in the 'jwst_miri_specwcs_0005.fits' reference file) is in good match with the known spectral features detected in our spectra.

Data quality. The spectra from all three instruments are shown in Fig. 2 for the A_V = 60 mag star. The flux calibration of these data is such that they match each other within their respective 3σ error bars. The differences in the signal at the bottom of the 3 μm H_2O feature are due to the increased sensitivity of NIRSPEC FS relative to NIRCAM WFSS, but are within the error bars. Both stars are saturated in the 4.3 μm $^{12}CO_2$ ice bands and we lose the signal at the bottom of these features, which occurs as well in the 3 μm band of the A_V = 95 mag star. The reproducibility of the spectral features between NIRCam and NIRSpec is excellent, and the spectra are broadly consistent with the Spitzer Infrared Array Camera (IRAC) photometry of this source given in the Spitzer Enhanced Imaging Products (SEIP) Source List server (https://irsa.ipac.caltech.edu/cgi-bin/Gator/nph-dd), taking into account the lack of convolution with the IRAC filter and the assumed colour correction.

Global continuum fit. The continuum shape of background stars, which is physically limited to be a stellar Rayleigh Jeans tail with ices superimposed on it, is fitted either with detailed stellar photosphere models or simple piece-wise polynomial continua to each star[44]. We do not yet have photospheric models for these stars, so we use polynomial fits: in our case, one over the NIRSpec range and another over the MIRI range. For NIR38 (A_V = 60 mag), we fit the continuum using a fifth-order polynomial with continuum points of 2.4–2.49 μm, 2.65–2.69 μm, 2.715–2.720 μm, 4.0–4.04 μm, 4.06–4.07 μm, 5.15–5.2 μm and 5.3–5.7 μm. For J110621 (A_V = 95 mag), we fit the following continuum points: 2.74–2.78 μm, 3.98–4.01 μm and 5.4–5.7 μm. The continuum determination in the MIRI LRS range is not straightforward due to the broad ice and silicate features. We determine the continuum on the MIRI LRS range (5.2–13 μm) using a second-order polynomial function. We set the continuum points at 5.2 μm, 5.6 μm and 13.2 μm for NIR38 and J110621. Then we combine the two continua in a piece-wise fashion, with the cut-off between them taken at 5.1 μm. The continuum shape may change slightly when the more detail stellar model is applied. However, our initial steps in stellar modelling (not discussed here) show good agreement with the polynomial continuum fit found here. We estimate that the uncertainty introduced by the continuum is within the uncertainty in the A values used to derive the column densities.

The silicate absorption band is removed by a synthetic silicate spectrum composed of amorphous pyroxene[45] ($Mg_{0.7}Fe_{0.3}SiO_3$) and olivine[45] ($MgFeSiO_4$), as previously used in the literature[44] for background stars (Extended Data Fig. 6). We used the optool code[46] to create a synthetic spectrum assuming grains of 1 μm. We aim at matching the spectral ranges between 8.3 μm and 8.7 μm and between 10.1 μm and 10.4 μm. In both sources, the absorption of pyroxene dominates over olivine at 9.8 μm. For the A_V = 60 mag star, pyroxene and olivine corresponds to 60% and 40%, respectively, whereas for the the A_V = 95 mag star, the absorptions are 70% due to pyroxene and 30% due to olivine.

ENIIGMA global fitting and local fits. We used the ENIIGMA fitting tool[47,48] to simultaneously fit multiple features across the NIRSpec and MIRI/LRS range by scaling laboratory ice spectra to match the optical depths in Fig. 1. A full list with data used in this paper is shown in Table 3. It is worth mentioning that these laboratory data are previously baseline corrected and noise smoothed at relevant bands. No further processing is performed during the fitting procedure. In the fits, we assume saturated bands at 3 μm and 4.27 μm because of negative fluxes. At these two bands, the fit is not limited by the peak of the band. This is an important assumption to make to avoid underestimating column densities of the molecules contributing to the absorption of these bands. ENIIGMA searched for the best combination of experimental data measured at temperatures of 15 K or below. Motivated by previous studies, we explored combinations with ice mixtures composed of CO:CO_2 (ref. [49]), CO:CH_3OH (ref. [50]), H_2O:CH_3OH (ref. [51]) and H_2O:NH_3 (ref. [30]), H_2O:CO_2:CH_4 (ref. [52]) and pure CO (ref. [53]). In addition to these data, ENIIGMA tested other infrared spectra measured at temperatures below 16 K. We did not include the spectrum of the ammonium ion (NH_4^+) in the global fits because it is not a consensus that the 6.85 μm is attributed to this chemical species. A dedicated study of this spectral feature will be performed in a follow-up paper by considering different chemical environments where NH_4^+ could exist. In addition, as NH_4^+ is formed by a chemical reaction between other molecules (for example, NH_3, HNCO) induced by temperature (warm-up) or radiation (for example, ultraviolet, X-rays, cosmic rays), the spectrum shows other products that have to be taken into account when making assignments of the infrared bands. Overall, ENIIGMA provides a good global fit of the major ice components in the observations, which are used to derive the ice column densities (Table 2). They are calculated by $N_X = \int \tau_\nu d\nu / A$, where $\int \tau_\nu d\nu$ is the integrated optical depth of a specific band, A is the band strength and X is the chemical species. The uncertainties are derived from 3σ confidence intervals based on correlation plots shown in Extended Data Fig. 3. Additional sources of uncertainties are not considered in these values. ENIIGMA does not fit entirely the isotope bands of $^{13}CO_2$ and ^{13}CO at 4.38 μm and 4.78 μm, respectively. First, this is because the global fit limits the amount of the isotopes by the strong $^{12}CO_2$ and ^{12}CO bands. Second, the isotope abundances in the gases used to make the ice samples in the laboratory may not be the same as found in these astronomical targets. By performing local fits, the chemistry of the isotope bands is better constrained (Extended Data Fig. 4). Nevertheless, the ice column densities are similar to the values obtained with the global fits as seen in Table 2.

Local fits are also used to calculate the ice column densities of the major components (Supplementary Fig. 1). For the H_2O ice, we scale the pure H_2O ice infrared spectrum at 15 K (ref. [54]) to match the ranges around 2.85–2.95 μm and 3.17–3.23 μm because of the saturation of

Table 3 | Laboratory data tested in the global fit performed with ENIIGMA

Label	Temperature (K)	Database/ reference
H_2O	15	LIDA[4]
NH_3	10	LIDA[79]
CH_4	10	LIDA[33]
CO	12	LIDA[62]
CO_2	12	LIDA[62]
CH_3OH	10	LIDA[31]
NH_3:CH_3OH (1:1)	12	UNIVAP[47]
H_2O:NH_3 (10:1.6)	10	–
H_2O:CO_2 (10:1)	10	LIDA[60]
H_2O:CO_2 (1:10)	10	LIDA[60]
H_2O:CO_2 (1:6)	10	LIDA[60]
H_2O:CO_2 (1:1)	10	LIDA[60]
H_2O:CO (20:1)	16	NASA/Ames[80]
H_2O:CH_4 (20:1)	15	NASA/Ames[80]
H_2O:CO_2:CH_4 (10:1:1)	12	UNIVAP[81]
H_2O:CH_3OH:CO_2:CH_4 (0.6:0.7:1:0.1)	10	LIDA[61]
H_2O:CH_3OH:CO_2 (9:1:2)	10	LIDA[61]
H_2O:CH_3OH:CO:NH_3 (100:50:1:1)	10	NASA/Ames[57]
H_2O:CH_3OH (10:0.8)	10	–
CO_2:CH_3OH (1:1)	10	LIDA[60]
CO:CO_2 (1:1)	15	LIDA[62]
CO:CH_3OH (4:1)	15	LIDA[50]

LIDA, The Leiden Ice Database for Astrochemistry; UNIVAP, Universidade do Vale do Paraiba.

the bands. The broadband between 5 μm and 8 μm is fitted by NH_4^+ and H_2O as scaled to the 3 μm band. Independently of the global fit, the NH_4^+ spectrum can be locally scaled to the astronomical data as this method does not take into account the contribution of the chemical species at other wavelengths. The goal of the local fits is to estimate the highest amount of a specific component to the absorption band including or not blending effects with other molecules. As the contribution of CH_3OH absorption is minimal at 6.85 μm (Extended Data Figs. 1 and 2), we do not include methanol in the local fit of this band. In the cases of CO_2, CO, CH_4, SO_2, NH_3 and CH_3OH, we adopted Gaussian profiles to fit the A_V = 60 mag and A_V = 95 mag spectra, and calculate the ice column densities. Around 4.67 μm and 7.7 μm, we adopted more than one sub-component to fit the observations, following the previous studies of these two bands[52,53]. For CH_3OH, we also perform a local fit analysis around 3.5 μm, and the column densities are similar to both local and global fits at 9.8 μm. The local column densities are compared with the global column densities in Supplementary Information to validate the global fits.

The ice column densities derived from the global and local fit are collated in Table 2. In Fig. 4, we show the column densities of the major ice species derived from the global fits and the minor species derived from the local fits. In addition, we show a comparison with the column densities derived for a background star with A_V = 19 mag (ref. [55]). These column densities are normalized to H_2O ice in the bottom panel of Fig. 4. In Supplementary Information, all the values from global and local fits, and from the ranges reported in the literature are compared. A caveat in the ENIIGMA methodology, is that it does not perform grain shape correction of the ice bands. Such a correction comes with a level of discussion beyond the scope of this paper, for example, which grain shape better reproduces the observations, and what are the size distributions. These geometry effects will be explored in a subsequent study.

Local continuum fit for weak features. To separate the weaker features from the wing of the water stretch and combination bands, we also fit a local continuum to both spectra. The continuum points were set to the following ranges: 3.215–3.231 μm, 3.252–3.263 μm, 3.289–3.295 μm, 3.306–3.311 μm, 3.610–3.626 μm, 3.686–3.693 μm, 3.711–3.727 μm and 3.759–3.795 μm. We calculated a fifth-order polynomial to these regions and took the local optical depths with respect to this continuum. For ^{13}CO, CH_3OH, OCN^- and OCS we scaled laboratory data of simple ice mixtures to match the feature profiles. The profile of the best-fitting scaled laboratory mixture and band strengths were used to determine local column densities, as described below.

3.4–3.6 μm blended absorption (CH_3OH and $NH_3{\cdot}H_2O$). The absorption feature between ~3.35 μm and 3.6 μm is probably caused by a combination of different ices and grain properties. However, there is a distinct peak at 3.53 μm for both sources, indicating the presence of CH_3OH ice (C–H stretching mode)[16]. To constrain the CH_3OH ice abundance, we used the fifth-order polynomial local baseline described above to obtain the optical depths for this feature. Previous studies have fit a simple Gaussian to CH_3OH along lines of sight towards background stars but this underestimates the red wing in the feature for both lines of sight in this study[44,56]. We therefore scaled laboratory spectra of pure CH_3OH ice at 15 K (ref. [31]) to fit the region and minimize the residuals between 3.53 μm and 3.65 μm. We did not fit the laboratory data to shorter wavelengths because the use of a local baseline instead of a global baseline cuts off some of the CH_3OH ice profile. Additional absorbing species and scattering signatures may contribute to this absorption feature. The column densities are calculated by integrating the scaled laboratory optical depths using a band strength $A_{CH3OH} = 1.6 \times 10^{-16}$ cm per molecule over the 2.778–3.704 μm regime[57] and represent upper limits to the amount of methanol present, due to the potential for additional absorption described above. These results are presented in Table 2 as upper limits, and the fits for both sources are shown in Extended Data Fig. 9.

The peak near ~3.47 μm has been previously attributed to the $NH_3{\cdot}H_2O$ hydrates but this is still up for debate[30,58]. Nonetheless, we model the feature using a simple Gaussian at this time with a full-width at half-maximum (FWHM) of 0.1 μm and a central peak at 3.47 μm to understand how much this overlapping feature may reduce the column density of the CH_3OH. We model the Gaussian and lab data simultaneously and minimize the residuals of the sum of both fits between 3.4–3.65 μm (Extended Data Fig. 9). When doing this, we find that the column densities for CH_3OH are lower by ~20–30% ($N = 4.1 \times 10^{17}$ cm^{-2} and $N = 4.5 \times 10^{17}$–cm^{-2} for the A_V = 60 mag and A_V = 95 mag sources, respectively). These column densities agree with those found by using the ENIIGMA fits to the globally determined optical depths. Further follow-up studies will model the full 3.4–3.6 μm absorption feature and constrain the column densities for not only CH_3OH but also the other possible absorbing species.

$^{13}CO_2$. Extended Data Fig. 4 shows the observed $^{13}CO_2$ feature, around 4.39 μm, compared with laboratory spectra of CO_2 in different ice mixtures, which peak at slightly different wavelengths depending on the ice mixture. The peak of each laboratory spectrum is scaled to the observed $^{13}CO_2$ feature at the wavelength corresponding to the peak of the laboratory data. Overall, the band of $^{13}CO_2$ in H_2O-rich ice reproduces the peak and width of the observed feature. A weak blue shoulder around 4.384 μm is also noticeable and could possibly be due to a fraction of $^{13}CO_2$ mixed in CO. A detailed study of the components that contribute to the 4.39 μm feature, combined with an analysis of the CO_2 bands, can provide more insights about the formation and chemical environment of solid CO_2 and its ^{13}C isotopologue, and it will be the focus of a future work. In this work, we provide an estimate of the $^{13}CO_2$ column density assuming that the 4.39 μm band can be modelled using the laboratory spectrum of a CO_2:H_2O (1:10) ice at 10 K. The column density of $^{13}CO_2$ is derived by scaling the laboratory spectrum to the optical depth of the 4.39 μm feature. A band strength of $A = 7.8 \times 10^{-17}$ cm per molecule[59] is assumed for $^{13}CO_2$ asymmetric stretching. The laboratory data used for the comparison are taken from refs. [60,61]. In these laboratory ices, $^{13}CO_2$ is set at a ratio of $^{12}CO_2/^{13}CO_2 \approx 90$, which need not be the same ratio in the astronomical targets. To calculate this ratio from the astronomical data, we divide the column densities derived with ENIIGMA for the $^{12}CO_2$ feature by those derived here for the $^{13}CO_2$ feature, yielding a ratio of $^{12}CO_2/^{13}CO_2 \approx 69$–$87$ for these two targets.

OCN^-. In our analysis of the XCN band a single-component fit is used and plotted in Extended Data Fig. 7. This is a Gaussian function with peak centre at 2,165.9 cm^{-1} and FWHM = 23 cm^{-1} previously used to reproduce laboratory spectra of OCN^- (ref. [62]) and the XCN band of embedded young stellar objects[17,63–65]. Only data points on the blue wing of the XCN band are considered to avoid any contributions from the CO-ice band to the fit. The Gaussian profile reproduces the red wing and the component of the XCN band of both targets. In addition, the residuals are negligible, justifying the use of a single component. OCN^- ice column densities were estimated by integrating over the fitted Gaussian function and scaling with a band strength A_{OCN^-} of 1.3×10^{-16} cm per molecule[62]. The resulting column densities are listed in Table 2, and they are in good agreement with values obtained for quiescent lines of sight in nearby clouds[64].

^{13}CO. The region around 4.779 μm shows a weak feature that can be associated with ^{13}CO (Extended Data Fig. 5). This feature is contaminated by the presence of photospheric absorption lines, which makes the feature difficult to integrate cleanly. For this reason, the laboratory spectrum of pure CO ice at 15 K (ref. [66]) was scaled to the astronomical data to derive the maximum abundance of this species in the spectra of both background stars. The band strength value is $A = 1.3 \times 10^{-17}$ cm per molecule[59].

OCS. The region around 4.90 μm shows tentative detection that can be associated with the CO stretching vibration of the OCS molecule (Extended Data Fig. 8). A comparison with laboratory infrared spectra of OCS-containing ices shows that this band in pure OCS ice is too broad compared with the feature seen towards the background stars. Previous studies have shown that this absorption band is better modelled by CH_3OH:OCS-containing ices[67,68]. The column densities for OCS were derived using the profile of the OCS mixed in H_2O and a band strength value of $A = 1.18 \times 10^{-16}$ cm per molecule[69].

Non-detections and upper limits. With these high S/N data, we have placed strong constraints on several ice species, including HDO, HCN, CH_3CN, H_2CO and H_2S. H_2CO may still be present at low levels in these spectra, but with the lower resolving power ($R \approx 100$) of MIRI LRS FS, it is not possible to separate it from the blue wing of the H_2O bending mode at 6 μm. In contrast, it was clearly detected in a protostar with JWST's MIRI MRS mode ($R \approx 3{,}000$)[32]. HDO was tentatively detected with Akari at ~4.1 μm with an abundance of 2–10% relative to H_2O towards several protostars and disks[15]. We do not see an obvious feature there in these spectra, although reliable upper limits can only be obtained after correction for the $^{12}CO_2$ blue scattering emission wing. Upper limits for the H_2S, CH_3CN and HCN abundances are estimated considering the noise level in the region where the strongest vibrational feature of these molecules absorb. Here, the regions around 3.92 μm, 4.44 μm and 4.76 μm for H_2S, CH_3CN and HCN, respectively. The upper limits are calculated from the root mean squared (RMS) as $N = \mathrm{RMS} \times \mathrm{FWHM}/A$, where A is the band strength of the absorption feature in the pure ice. The resulting 1σ upper limits in the abundances with respect to H_2O ice is less than 1% for H_2S in NIR38. Data covering this region are not yet available for J110621. For HCN, the upper limits with respect to H_2O ice is less than 1% for both sources. For CH_3CN the value is less than 2% for both sources. The FWHM and band strengths for the pure ices are taken from refs. [69–71].

The location of the background stars in their larger-scale environments. Complementary information about the larger-scale environment is critical when interpreting the column densities inferred from the ice observations. Extended Data Fig. 10 shows a map of the H_2 column density maps extracted from the larger-scale Chamaeleon maps[72] created based on far-infrared data 70 μm to 500 μm from the Herschel Space Observatory's Gould Belt survey[73]. The maps clearly show the decrease of the column density from the peak near the class 0 protostar ChamI-MMS with a more extended structure encompassing also the clump Cha1-C2 (ref. [18]). The $A_V \approx 95$ mag star at a projected distance of 6,600 au is located in the direction of this core, while the $A_V \approx 60$ mag star at a projected distance of 5,600 au is located in a direction orthogonal to this structure from the class 0 protostar[20]. The H_2 column densities toward the two background stars are similar within ~10%, suggesting that the local conditions are similar, despite the difference in A_V. The A_V we use was derived from average giant star colours[20]; from these JWST spectra, a more detailed fit taking into account the spectral type of these background stars will soon be possible, which may reduce the difference in A_V. If the discrepancy remains, the difference in A_V could represent local radial extensions of the cloud along the line of sight or a superposition of additional clouds along the line of sight. Complementary observations, for example of gas-phase line tracers, are needed to assess whether there are differences in the densities, and thereby, for example, the timescales for freeze-out, towards the two differ significantly.

Calculation of the icy C, O, N and S budgets. The column of molecular hydrogen is calculated for each line of sight as $N_{H2} \approx 1.0 \times 10^{21}\ \mathrm{cm}^{-2}\ A_V$ (ref. [74]). Assuming cosmic abundances for the combined volatile and refractory abundances in the interstellar medium[75], the molecular hydrogen column can be converted into expected bulk budgets of C, O, N and S. To determine what fraction of these budgets our ices represent, we summed the column densities of all C-bearing, O-bearing, N-bearing and S-bearing ice species. For the O-bearing species, we doubled the column densities of $^{12}CO_2$, $^{13}CO_2$ and SO_2 to account for the two oxygen atoms. For both NIR38 and J110621, we see only 19% of the total O budget, 19% and 14%, respectively, of the C budget, and 13% of the N budget and 1% of the S budget for both. If we assume the N_{H2}/N_{CO} conversion for molecular clouds[74], then the expected amount of total CO towards NIR38 and J110621 are $1.08 \times 10^{19}\ \mathrm{cm}^{-2}$ and $1.71 \times 10^{19}\ \mathrm{cm}^{-2}$, respectively.

Data availability

Our raw data are publicly available at the STScI MAST JWST archive. Text files of our enhanced one-dimensional spectra are provided as part of our Early Release Science enabling product deliverables on Zenodo at the following URL: https://doi.org/10.5281/zenodo.7501239.

Code availability

The ENIIGMA global fitting tool[47] is publicly available on GitHub at https://github.com/willastro/ENIIGMA-fitting-tool.

References

1. Dulieu, F. et al. Experimental evidence for water formation on interstellar dust grains by hydrogen and oxygen atoms. *Astron. Astrophys.* **512**, A30 (2010).
2. Ioppolo, S., Cuppen, H., Romanzin, C., van Dishoeck, E. & Linnartz, H. Laboratory evidence for efficient water formation in interstellar ices. *Astrophys. J.* **686**, 1474 (2008).
3. Qasim, D. et al. An experimental study of the surface formation of methane in interstellar molecular clouds. *Nat. Astron.* **4**, 781–785 (2020).
4. Lamberts, T. et al. Methane formation in cold regions from carbon atoms and molecular hydrogen. *Astrophys. J.* **928**, 48 (2022).
5. Hiraoka, K. et al. Ammonia formation from the reactions of H atoms with N atoms trapped in a solid N_2 matrix at 10–30 K. *Astrophys. J.* **443**, 363–370 (1995).
6. Fedoseev, G., Ioppolo, S. & Linnartz, H. Deuterium enrichment of ammonia produced by surface N + H/D addition reactions at low temperature. *Mon. Not. R. Astron. Soc.* **446**, 449–458 (2015).
7. Caselli, P., Walmsley, C., Tafalla, M., Dore, L. & Myers, P. CO depletion in the starless cloud core L1544. *Astrophys. J.* **523**, L165 (1999).
8. Pontoppidan, K. M. Spatial mapping of ices in the Ophiuchus-F core—a direct measurement of CO depletion and the formation of CO_2. *Astron. Astrophys.* **453**, L47–L50 (2006).
9. Watanabe, N. & Kouchi, A. Measurements of conversion rates of CO to CO_2 in ultraviolet-induced reaction of $D_2O(H_2O)$/CO amorphous ice. *Astrophys. J.* **567**, 651 (2002).
10. Chuang, K.-J., Fedoseev, G., Ioppolo, S., van Dishoeck, E. & Linnartz, H. H-atom addition and abstraction reactions in mixed CO, H_2CO and CH_3OH ices—an extended view on complex organic molecule formation. *Mon. Not. R. Astron. Soc.* **455**, 1702–1712 (2016).
11. Altwegg, K. et al. Prebiotic chemicals-amino acid and phosphorus-in the coma of comet 67P/Churyumov–Gerasimenko. *Sci. Adv.* **2**, e1600285 (2016).
12. Ioppolo, S. et al. A non-energetic mechanism for glycine formation in the interstellar medium. *Nat. Astron.* **5**, 197–205 (2021).
13. Gibb, E. L. et al. Interstellar ice: the Infrared Space Observatory legacy. *Astrophys. J. Suppl. Ser.* **151**, 35 (2004).
14. Boogert, A. et al. The c2d Spitzer Spectroscopic Survey of ices around low-mass young stellar objects. I. H_2O and the 5–8 μm bands. *Astrophys. J.* **678**, 985 (2008).
15. Aikawa, Y. et al. Akari observations of ice absorption bands towards edge-on young stellar objects. *Astron. Astrophys.* **538**, A57 (2012).

16. Boogert, A., Gerakines, P. A. & Whittet, D. C. Observations of the icy universe. *Annu. Rev. Astron. Astrophys.* **53**, 541–581 (2015).
17. Noble, J., Fraser, H., Pontoppidan, K. & Craigon, A. Two-dimensional ice mapping of molecular cores. *Mon. Not. R. Astron. Soc.* **467**, 4753–4762 (2017).
18. Belloche, A. et al. The end of star formation in Chamaeleon I? A LABOCA census of starless and protostellar cores. *Astron. Astrophys.* **527**, A145 (2011).
19. Dzib, S. A., Loinard, L., Ortiz-León, G. N., Rodríguez, L. F. & Galli, P. A. Distances and kinematics of Gould Belt star-forming regions with Gaia DR2 results. *Astrophys. J.* **867**, 151 (2018).
20. Jin, M. et al. Ice Age: chemodynamical modeling of Cha-MMS1 to predict new solid-phase species for detection with JWST. *Astrophys. J.* **935**, 133 (2022).
21. Jakobsen, P. et al. The near-infrared spectrograph (NIRSpec) on the James Webb Space Telescope—I. overview of the instrument and its capabilities. *Astron. Astrophys.* **661**, A80 (2022).
22. Greene, T. P. et al. λ = 2.4 to 5 μm spectroscopy with the James Webb Space Telescope NIRCam instrument. *J. Astron. Telesc. Instrum. Syst.* **3**, 035001 (2017).
23. Rieke, G. H. et al. The mid-infrared instrument for the James Webb Space Telescope, I: introduction. *Publ. Astron. Soc. Pac.* **127**, 584 (2015).
24. Dartois, E., Noble, J. A., Ysard, N., Demyk, K. & Chabot, M. Influence of grain growth on CO_2 ice spectroscopic profiles: modelling for dense cores and disks. *Astron. Astrophys.* **666**, A153 (2022).
25. Mumma, M. J. & Charnley, S. B. The chemical composition of comets-emerging taxonomies and natal heritage. *Annu. Rev. Astron. Astrophys.* **49**, 471–524 (2011).
26. Ferrante, R. F., Moore, M. H., Spiliotis, M. M. & Hudson, R. L. Formation of interstellar OCS: radiation chemistry and IR spectra of precursor ices. *Astrophys. J.* **684**, 1210 (2008).
27. Laas, J. C. & Caselli, P. Modeling sulfur depletion in interstellar clouds. *Astron. Astrophys.* **624**, A108 (2019).
28. Köhler, M., Jones, A. & Ysard, N. A hidden reservoir of Fe/FeS in interstellar silicates? *Astron. Astrophys.* **565**, L9 (2014).
29. Calmonte, U. et al. Sulphur-bearing species in the coma of comet 67P/Churyumov–Gerasimenko. *Mon. Not. R. Astron. Soc.* **462**, S253–S273 (2016).
30. Dartois, E. & d'Hendecourt, L. Search for NH_3 ice in cold dust envelopes around YSOs. *Astron. Astrophys.* **365**, 144–156 (2001).
31. van Scheltinga, J. T., Ligterink, N., Boogert, A., van Dishoeck, E. & Linnartz, H. Infrared spectra of complex organic molecules in astronomically relevant ice matrices—I. acetaldehyde, ethanol, and dimethyl ether. *Astron. Astrophys.* **611**, A35 (2018).
32. Yang, Y.-L. et al. CORINOS I: JWST/MIRI spectroscopy and imaging of a class 0 protostar IRAS 15398-3359. *Astrophys. J. Lett.* **941**, L13 (2022).
33. Rachid, M. G. et al. Infrared spectra of complex organic molecules in astronomically relevant ice mixtures. II. Acetone. *Astron. Astrophys.* **639**, A4 (2020).
34. Goumans, T., Uppal, M. A. & Brown, W. A. Formation of CO_2 on a carbonaceous surface: a quantum chemical study. *Mon. Not. R. Astron. Soc.* **384**, 1158–1164 (2008).
35. Garrod, R. T. & Pauly, T. On the formation of CO_2 and other interstellar ices. *Astrophys. J.* **735**, 15 (2011).
36. Qasim, D. et al. Formation of interstellar methanol ice prior to the heavy CO freeze-out stage. *Astron. Astrophys.* **612**, A83 (2018).
37. Molpeceres, G. et al. Carbon atom reactivity with amorphous solid water: H_2O-catalyzed formation of H_2CO. *J. Phys. Chem. Lett.* **12**, 10854–10860 (2021).
38. Brooke, T., Sellgren, K. & Smith, R. A study of absorption features in the 3 micron spectra of molecular cloud sources with H_2O ice bands. *Astrophys. J.* **459**, 209 (1996).
39. Silsbee, K., Ivlev, A. V., Sipilä, O., Caselli, P. & Zhao, B. Rapid elimination of small dust grains in molecular clouds. *Astron. Astrophys.* **641**, A39 (2020).
40. Ormel, C., Min, M., Tielens, A., Dominik, C. & Paszun, D. Dust coagulation and fragmentation in molecular clouds—II. The opacity of the dust aggregate size distribution. *Astron. Astrophys.* **532**, A43 (2011).
41. Horne, K. An optimal extraction algorithm for CCD spectroscopy. *Publ. Astron. Soc. Pac.* **98**, 609 (1986).
42. Sun, F. et al. First peek with JWST/NIRCam wide-field slitless spectroscopy: serendipitous discovery of a strong [O III]/Hα emitter at $z = 6.11$. *Astrophys. J. Lett.* **936**, L8 (2022).
43. Carnall, A. SpectRes: a fast spectral resampling tool in Python. Preprint at https://arxiv.org/abs/1705.05165 (2017).
44. Boogert, A. et al. Ice and dust in the quiescent medium of isolated dense cores. *Astrophys. J.* **729**, 92 (2011).
45. Dorschner, J., Begemann, B., Henning, T., Jaeger, C. & Mutschke, H. Steps toward interstellar silicate mineralogy. II. Study of Mg-Fe-silicate glasses of variable composition. *Astron. Astrophys.* **300**, 503 (1995).
46. Dominik, C., Min, M. & Tazaki, R. Optool: command-line driven tool for creating complex dust opacities. *Astrophysics Source Code Library* ascl:2104.010 (2021).
47. Rocha, W. R., Perotti, G., Kristensen, L. E. & Jørgensen, J. K. Fitting infrared ice spectra with genetic modelling algorithms-presenting the eniigma fitting tool. *Astron. Astrophys.* **654**, A158 (2021).
48. Rocha, W. et al. LIDA—the Leiden ice database for astrochemistry. *Astron. Astrophys.* **668**, A63 (2022).
49. Pontoppidan, K. M. et al. The c2d Spitzer Spectroscopic Survey of ices around low-mass young stellar objects. II. CO_2. *Astrophys. J.* **678**, 1005 (2008).
50. Cuppen, H., Penteado, E. & Isokoski, K. et al. CO ice mixed with CH_3OH: the answer to the non-detection of the 2152 cm^{-1} band? *Mon. Not. R. Astron. Soc.* **417**, 2809–2816 (2011).
51. Perotti, G. et al. Linking ice and gas in the Serpens low-mass star-forming region. *Astron. Astrophys.* **643**, A48 (2020).
52. Öberg, K. I. et al. The c2d Spitzer Spectroscopic Survey of ices around low-mass young stellar objects. III. CH_4. *Astrophys. J.* **678**, 1032 (2008).
53. Pontoppidan, K. et al. A μm VLT spectroscopic survey of embedded young low mass stars I—structure of the CO ice. *Astron. Astrophys.* **408**, 981–1007 (2003).
54. Öberg, K. I. et al. Effects of CO_2 on H_2O band profiles and band strengths in mixed H_2O:CO_2 ices. *Astron. Astrophys.* **462**, 1187–1198 (2007).
55. Knez, C. et al. Spitzer mid-infrared spectroscopy of ices toward extincted background stars. *Astrophys. J.* **635**, L145 (2005).
56. Chu, L. E., Hodapp, K. & Boogert, A. Observations of the onset of complex organic molecule formation in interstellar ices. *Astrophys. J.* **904**, 86 (2020).
57. Hudgins, D., Sandford, S., Allamandola, L. & Tielens, A. Mid-and far-infrared spectroscopy of ices-optical constants and integrated absorbances. *Astrophys. J. Suppl. Ser.* **86**, 713–870 (1993).
58. Shimonishi, T., Dartois, E., Onaka, T. & Boulanger, F. VLT/ISAAC infrared spectroscopy of embedded high-mass YSOs in the large magellanic cloud: methanol and the 3.47 μm band. *Astron. Astrophys.* **585**, A107 (2016).
59. Gerakines, P., Schutte, W., Greenberg, J. & van Dishoeck, E. F. The infrared band strengths of H_2O, CO and CO_2 in laboratory simulations of astrophysical ice mixtures. *Astron. Astrophys.* **296**, 810 (1995).
60. Ehrenfreund, P., Boogert, A., Gerakines, P., Tielens, A. & van Dishoeck, E. Infrared spectroscopy of interstellar apolar ice analogs. *Astron. Astrophys.* **328**, 649–669 (1997).

61. Ehrenfreund, P. et al. Laboratory studies of thermally processed H_2O–CH_3OH–CO_2 ice mixtures and their astrophysical implications. *Astron. Astrophys.* **350**, 240–253 (1999).
62. van Broekhuizen, F., Keane, J. & Schutte, W. A quantitative analysis of OCN^- formation in interstellar ice analogs. *Astron. Astrophys.* **415**, 425–436 (2004).
63. Pendleton, Y., Tielens, A., Tokunaga, A. & Bernstein, M. The interstellar 4.62 micron band. *Astrophys. J.* **513**, 294 (1999).
64. van Broekhuizen, F., Pontoppidan, K., Fraser, H. & van Dishoeck, E. A 3–5 μm VLT spectroscopic survey of embedded young low mass stars II—solid OCN. *Astron. Astrophys.* **441**, 249–260 (2005).
65. Noble, J. A. et al. The thermal reactivity of HCN and NH_3 in interstellar ice analogues. *Mon. Not. R. Astron. Soc.* **428**, 3262–3273 (2013).
66. van Broekhuizen, F., Groot, I., Fraser, H., van Dishoeck, E. & Schlemmer, S. Infrared spectroscopy of solid CO–CO_2 mixtures and layers. *Astron. Astrophys.* **451**, 723–731 (2006).
67. Palumbo, M., Tielens, A. & Tokunaga, A. T. Solid carbonyl sulphide (OCS) in W33A. *Astrophys. J.* **449**, 674 (1995).
68. Palumbo, M., Geballe, T. & Tielens, A. G. Solid carbonyl sulfide (OCS) in dense molecular clouds. *Astrophys. J.* **479**, 839 (1997).
69. Yarnall, Y. Y. & Hudson, R. L. A new method for measuring infrared band strengths in H_2O ices: first results for OCS, H_2S, and SO_2. *Astrophys. J. Lett.* **931**, L4 (2022).
70. Rachid, M. G., Rocha, W. & Linnartz, H. Infrared spectra of complex organic molecules in astronomically relevant ice mixtures—V. methyl cyanide (acetonitrile). *Astron. Astrophys.* **665**, A89 (2022).
71. Gerakines, P. A., Yarnall, Y. Y. & Hudson, R. L. Direct measurements of infrared intensities of HCN and H_2O + HCN ices for laboratory and observational astrochemistry. *Mon. Not. R. Astron. Soc.* **509**, 3515–3522 (2022).
72. de Oliveira, C. A. et al. Herschel view of the large-scale structure in the Chamaeleon dark clouds. *Astron. Astrophys.* **568**, A98 (2014).
73. André, P. et al. From filamentary clouds to prestellar cores to the stellar IMF: initial highlights from the Herschel Gould Belt Survey. *Astron. Astrophys.* **518**, L102 (2010).
74. Lacy, J. H., Sneden, C., Kim, H. & Jaffe, D. T. H_2, CO, and dust absorption through cold molecular clouds. *Astrophys. J.* **838**, 66 (2017).
75. Przybilla, N., Nieva, M.-F. & Butler, K. A cosmic abundance standard: chemical homogeneity of the solar neighborhood and the ISM dust-phase composition. *Astrophys. J.* **688**, L103 (2008).
76. Bouilloud, M. et al. Bibliographic review and new measurements of the infrared band strengths of pure molecules at 25 K: H_2O, CO_2, CO, CH_4, NH_3, CH_3OH, HCOOH and H_2CO. *Mon. Not. R. Astron. Soc.* **451**, 2145–2160 (2015).
77. Schutte, W. & Khanna, R. Origin of the 6.85 μm band near young stellar objects: the ammonium ion (NH_4^+) revisited. *Astron. Astrophys.* **398**, 1049–1062 (2003).
78. Boogert, A., Schutte, W., Helmich, F., Tielens, A. & Wooden, D. Infrared observations and laboratory simulations of interstellar CH_4 and SO_2. *Astron. Astrophys.* **317**, 929–941 (1997).
79. Taban, I. M. et al. Stringent upper limits to the solid NH_3 abundance towards W33A from near-IR spectroscopy with the Very Large Telescope. *Astron. Astrophys.* **399**, 169 (2003).
80. Hudson, R. L. & Moore, M. H. Laboratory studies of the formation of methanol and other organic molecules by water+carbon monoxide radiolysis: relevance to comets, icy satellites, and interstellar ices. *Icarus* **140**, 451 (1999).
81. Rocha, W. R. M. et al. Infrared complex refractive index of astrophysical ices exposed to cosmic rays simulated in the laboratory. *Mon. Not. R. Astron. Soc.* **464**, 754 (2017).

Acknowledgements

The Ice Age Early Release Science team thanks the support team at STScI (W. Januszewski, B. Sargent, N. Pirzkal and M. Engesser) for their technical suggestions and improvements to the programme since 2017. M.K.M. acknowledges financial support from the Dutch Research Council (NWO; grant VI.Veni.192.241). M.G.R. acknowleges support from the Netherlands Research School for Astronomy (NOVA). S.I., H.L. and E.F.v.D. acknowledge support from the Danish National Research Foundation through the Center of Excellence 'InterCat' (grant agreement number DNRF150). E.F.v.D. acknowledges support from ERC grant 101019751 MOLDISK. The research of L.E.K. is supported by a research grant (19127) from VILLUM FONDEN. Part of this research was carried out at the Jet Propulsion Laboratory, California Institute of Technology, under a contract with the National Aeronautics and Space Administration (D.C.L.). F.S. acknowledges funding from JWST/NIRCam contract to the University of Arizona, NAS5-02105. A.C.A.B. acknowledges support from the Space Telescope Science Institute for programme JWST-ERS-01309.019. J.E. acknowledges support from the Space Telescope Science Institute for programme JWST-ERS-01309.019. L.E.U.C.'s research was supported by an appointment to the NASA Postdoctoral Program at the NASA Ames Research Center, administered by Oak Ridge Associated Universities under contract with NASA. D.H. is supported by Center for Informatics and Computation in Astronomy (CICA) grant and grant number 110J0353I9 from the Ministry of Education of Taiwan. D.H. acknowledges support from the National Technology and Science Council of Taiwan through grant number 111B3005191. M.N.D. acknowledges the Swiss National Science Foundation (SNSF) Ambizione grant number 180079, the Center for Space and Habitability (CSH) Fellowship, and the IAU Gruber Foundation Fellowship. I.J.-S. acknowledges financial support from grant number PID2019-105552RB-C41 by the Spanish Ministry of Science and Innovation/State Agency of Research MCIN/AEI/10.13039/501100011033. This work was supported by a grant from the Simons Foundation (686302, K.I.Ö.) and an award from the Simons Foundation (321183FY19, K.I.Ö.). J.K.J. acknowledges support from the Independent Research Fund Denmark (grant number 0135-00123B). Z.L.S. acknowledges financial support from the Royal Astronomical Society through the E. A. Milne Travelling Fellowship. J.A.N. and E.D. acknowledge support from French Programme National 'Physique et Chimie du Milieu Interstellaire' (PCMI) of the CNRS/INSU with the INC/INP, co-funded by the CEA and the CNES.

Author contributions

M.K.M. originated the proposal, designed the observations, co-managed the team, determined the feature optical depths and wrote much of the main text. W.R.M.R. performed global and local fitting to determine the column densities, including the error analysis, and wrote part of the Methods section. K.M.P. contributed to the observational design, reduced and optimized the NIRSpec data, wrote part of the Methods section and commented on the draft. N.C. reduced and optimized the MIRI LRS data to allow for the global fitting and wrote part of the Methods section. L.E.U.C. performed the local fitting of the methanol + hydrates band, wrote part of the Methods section and commented on the draft. E.D. wrote part of the discussion and made suggestions for the analysis. T.L. wrote portions of the results section and reorganized the draft. J.A.N. contributed to the original proposal, wrote portions of results section and made suggestions for the analysis. Y.J.P. managed the Overleaf file, wrote part of the results section and made suggestions for the local fitting. G.P. locally fit the OCN^- feature, wrote part of the Methods section and commented on the draft. D.Q. managed the Overleaf file and suggested parts of the

results and discussion sections. M.G.R. did the local fitting of the $^{13}CO_2$, ^{13}CO and OCS features, determined the upper limits and wrote part of the Methods section. Z.L.S. and F.S. reduced the NIRCam data, with contributions to the reduction scripts from H.D., and wrote part of the Methods section. T.L.B. benchmarked the NIRSpec spectra to validate them. A.C.A.B. helped to design the original programme, co-managed the team, organized the NIRCam analysis and commented on the draft. W.A.B., P.C., S.B.C., H.M.C., M.N.D., E.E., J.E., H.F., R.T.G., D.H., S.I., I.J.-S., M.J., J.K.J., L.E.K., D.C.L., M.R.S.M., B.A.M., G.J.M., K.I.Ö., M.E.P., T.S., J.A.S., E.F.v.D. and H.L. commented on the draft. Z.L.S., F.S., E.E., J.E., H.F. and T.S. also contributed to the observational design and analysis of the NIRCam data. H.L. helped motivate the original proposal, co-managed the team and organized the laboratory data used for the analysis. All authors participated in discussion of the observations, analysis and interpretation of the results.

Competing interests
The authors declare no competing interests.

Additional information
Extended data is available for this paper at https://doi.org/10.1038/s41550-022-01875-w.

Supplementary information The online version contains supplementary material available at https://doi.org/10.1038/s41550-022-01875-w.

Correspondence and requests for materials should be addressed to M. K. McClure.

Peer review information *Nature Astronomy* thanks the anonymous reviewers for their contribution to the peer review of this work

Reprints and permissions information is available at www.nature.com/reprints.

Publisher's note Springer Nature remains neutral with regard to jurisdictional claims in published maps and institutional affiliations.

[1]Leiden Observatory, Leiden University, Leiden, the Netherlands. [2]Laboratory for Astrophysics, Leiden Observatory, Leiden University, Leiden, the Netherlands. [3]Space Telescope Science Institute, Baltimore, MD, USA. [4]NASA Postdoctoral Program Fellow, NASA Ames Research Center, Moffett Field, CA, USA. [5]Institut des Sciences Moléculaires d'Orsay, CNRS, Université Paris-Saclay, Orsay, France. [6]Leiden Institute of Chemistry, Gorlaeus Laboratories, Leiden University, Leiden, the Netherlands. [7]Physique des Interactions Ioniques et Moléculaires, CNRS, Aix Marseille Université, Marseille, France. [8]Department of Physics, University of Central Florida, Orlando, FL, USA. [9]Max Planck Institute for Astronomy, Heidelberg, Germany. [10]Southwest Research Institute, San Antonio, TX, USA. [11]School of Physical Sciences, The Open University, Milton Keynes, UK. [12]Steward Observatory, University of Arizona, Tucson, AZ, USA. [13]Institute for Astronomy, University of Hawai'i at Manoa, Honolulu, HI, USA. [14]Department of Chemistry, University of Sussex, Brighton, UK. [15]Max-Planck-Institut für extraterrestrische Physik, Garching bei München, Germany. [16]Solar System Exploration Division, NASA Goddard Space Flight Center, Greenbelt, MD, USA. [17]Radboud University, Institute for Molecules and Materials, Nijmegen, the Netherlands. [18]Center for Space and Habitability, Universität Bern, Bern, Switzerland. [19]Departments of Astronomy and Chemistry, University of Virginia, Charlottesville, VA, USA. [20]Institute of Astronomy, Department of Physics, National Tsing Hua University, Hsinchu, Taiwan. [21]Center for Interstellar Catalysis, Department of Physics and Astronomy, Aarhus University, Aarhus, Denmark. [22]Centro de Astrobiología (CAB), CSIC-INTA, Torrejón de Ardoz, Spain. [23]Department of Physics, Catholic University of America, Washington DC, USA. [24]Niels Bohr Institute, University of Copenhagen, Copenhagen, Denmark. [25]Jet Propulsion Laboratory, California Institute of Technology, Pasadena, CA, USA. [26]Institute of Chemical Sciences, Heriot-Watt University, Edinburgh, Scotland. [27]Department of Chemistry, Massachusetts Institute of Technology, Cambridge, MA, USA. [28]National Radio Astronomy Observatory, Charlottesville, VA, USA. [29]Center for Astrophysics | Harvard & Smithsonian, Cambridge, MA, USA. [30]INAF - Osservatorio Astrofisico di Catania, Catania, Italy. [31]Faculty of Science, Niigata University, Niigata, Japan. ✉e-mail: mcclure@strw.leidenuniv.nl

https://doi.org/10.1038/s41550-022-01875-w

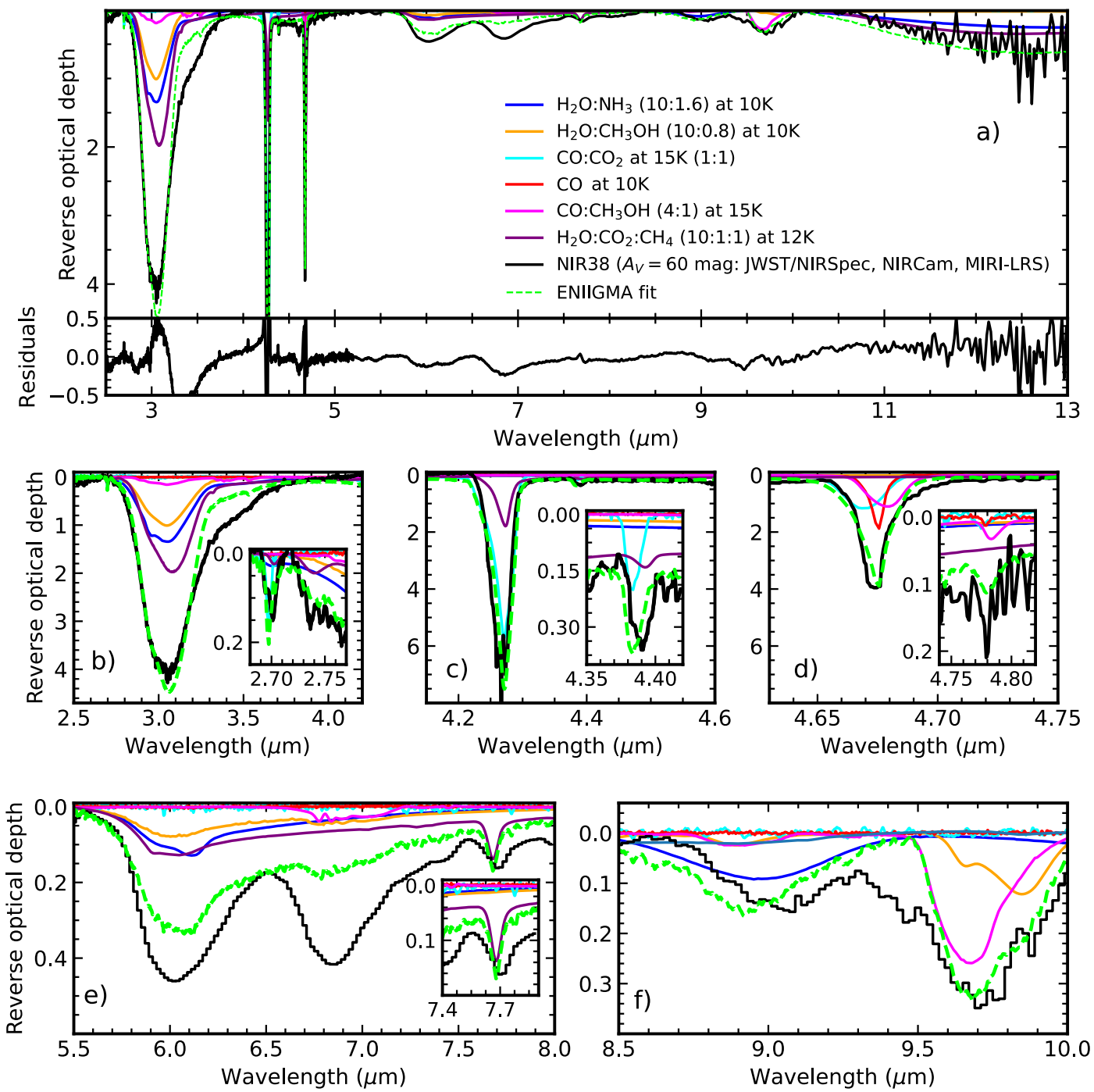

Extended Data Fig. 1 | Global fit of the combined spectrum for NIR38. Combined NIRSpec and MIRI/LRS spectrum of the NIR38 source (black), with the ENIIGMA fitting tool model (green). Each component in the fit is colour-coded. Panel *a* shows the entire range between 2.5 and 13 μm and the residuals of the fit. Panels *b-f* show a zoom-in of selected ranges corresponding to the major ice components. Small insets show the fit of $^{12}CO_2$ (Panel *b*), $^{13}CO_2$ (Panel *c*), ^{13}CO (panel *d*) and CH_4 (panel *e*).

https://doi.org/10.1038/s41550-022-01875-w

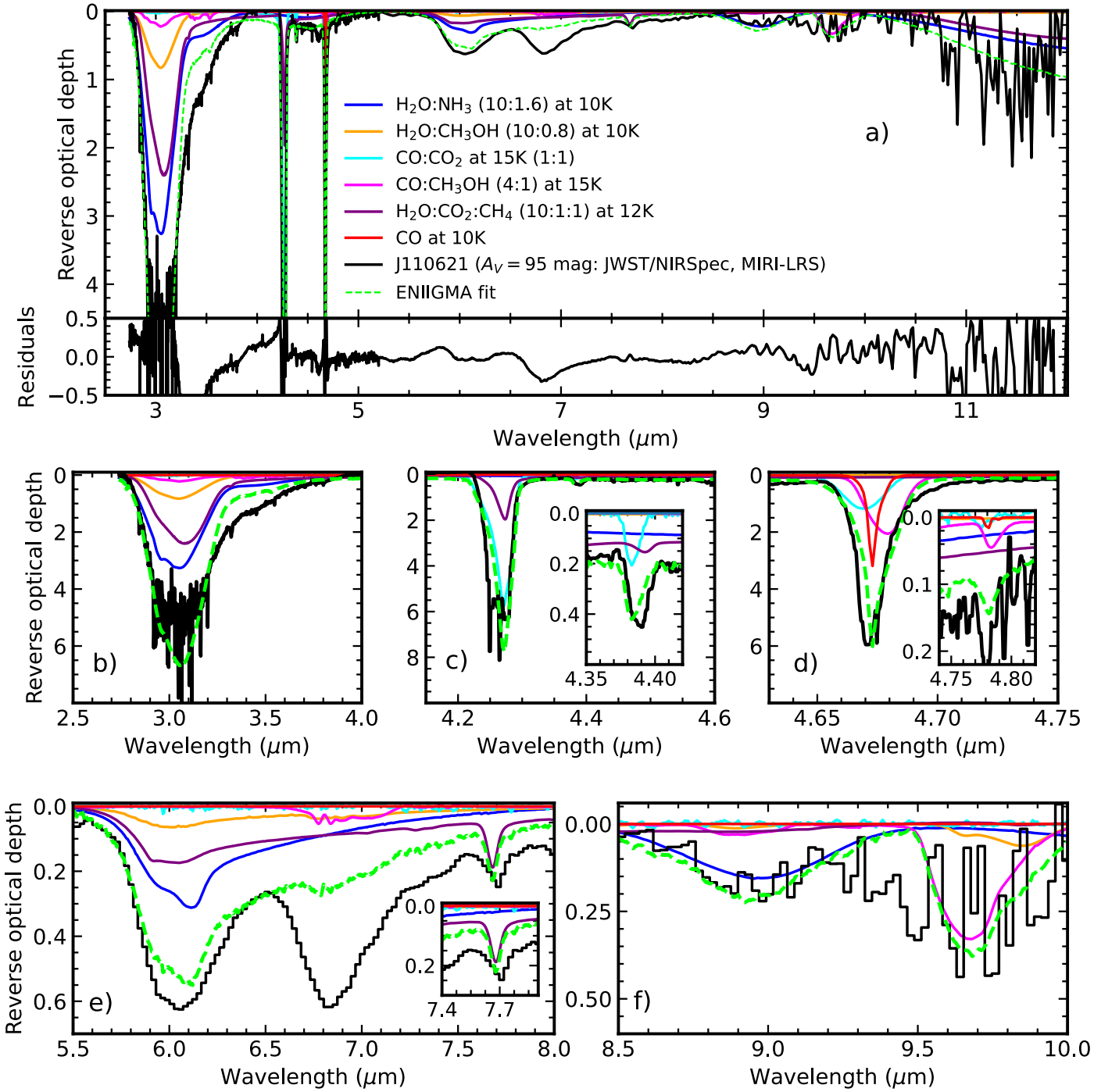

Extended Data Fig. 2 | Global fit of the combined spectrum for J110621. Combined NIRSpec and MIRI/LRS spectrum of the J110621 source (black), with the ENIIGMA fitting tool model (green). Each component in the fit is colour-coded. Panel *a* shows the entire range between 2.5 and 13 μm and the residuals of the fit. Panels *b-f* show a zoom-in of selected ranges corresponding to the major ice components. Small insets show the fit of $^{13}CO_2$ (Panel *c*), ^{13}CO (panel *d*) and CH_4 (panel *e*).

https://doi.org/10.1038/s41550-022-01875-w

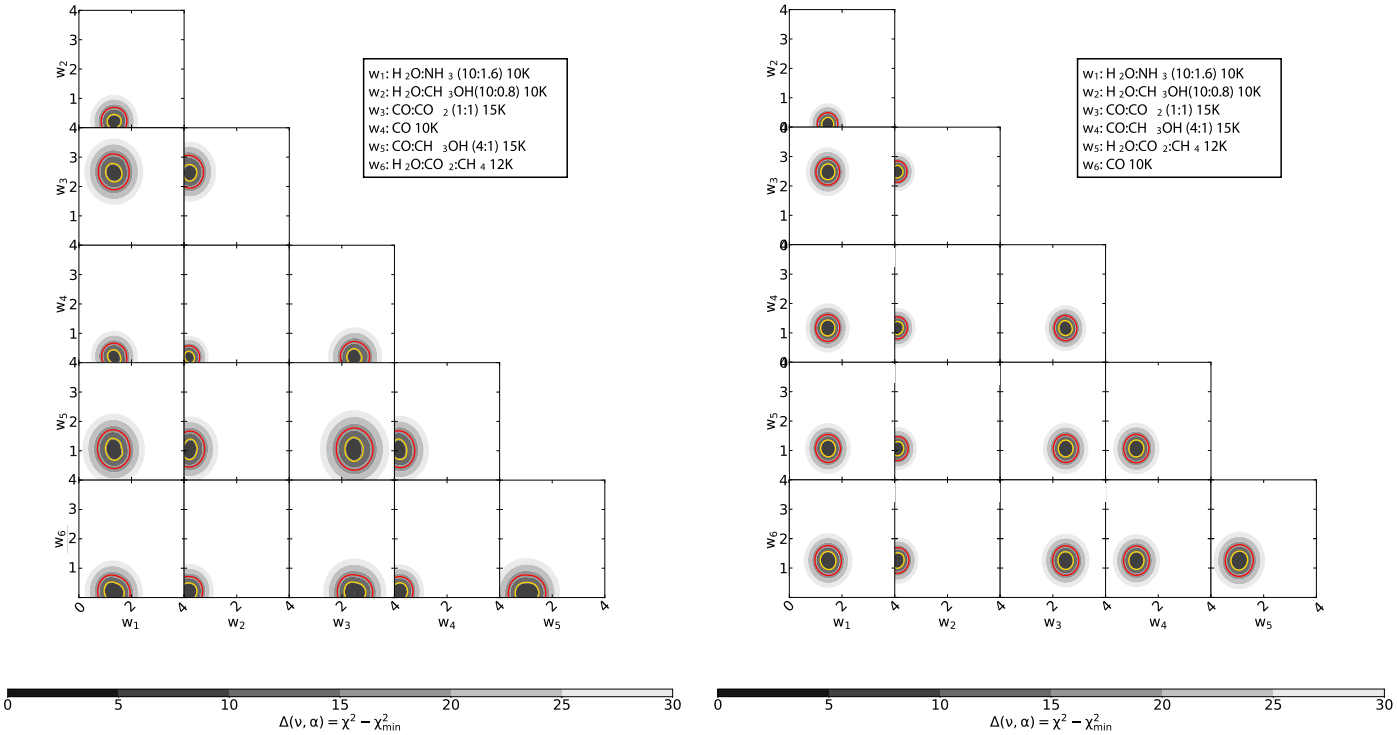

Extended Data Fig. 3 | Confidence interval analysis for the global fits to NIR38 and J110621. Corner plot showing the confidence interval analysis of the coefficients in the linear combination. The grey-scale contours show the differences in the χ^2 maps (Δ) which depends on the degree of freedom (ν) and the statistical significance (α). The yellow and red line contours indicate 2 and 3σ confidence intervals. The *left* and *right* plots are for NIR38 (A_V = 60 mag) and J110621 (A_V = 95 mag), respectively. Note that the ice species assigned to w1-w6 is automatically determined and differs between the left and right panels.

https://doi.org/10.1038/s41550-022-01875-w

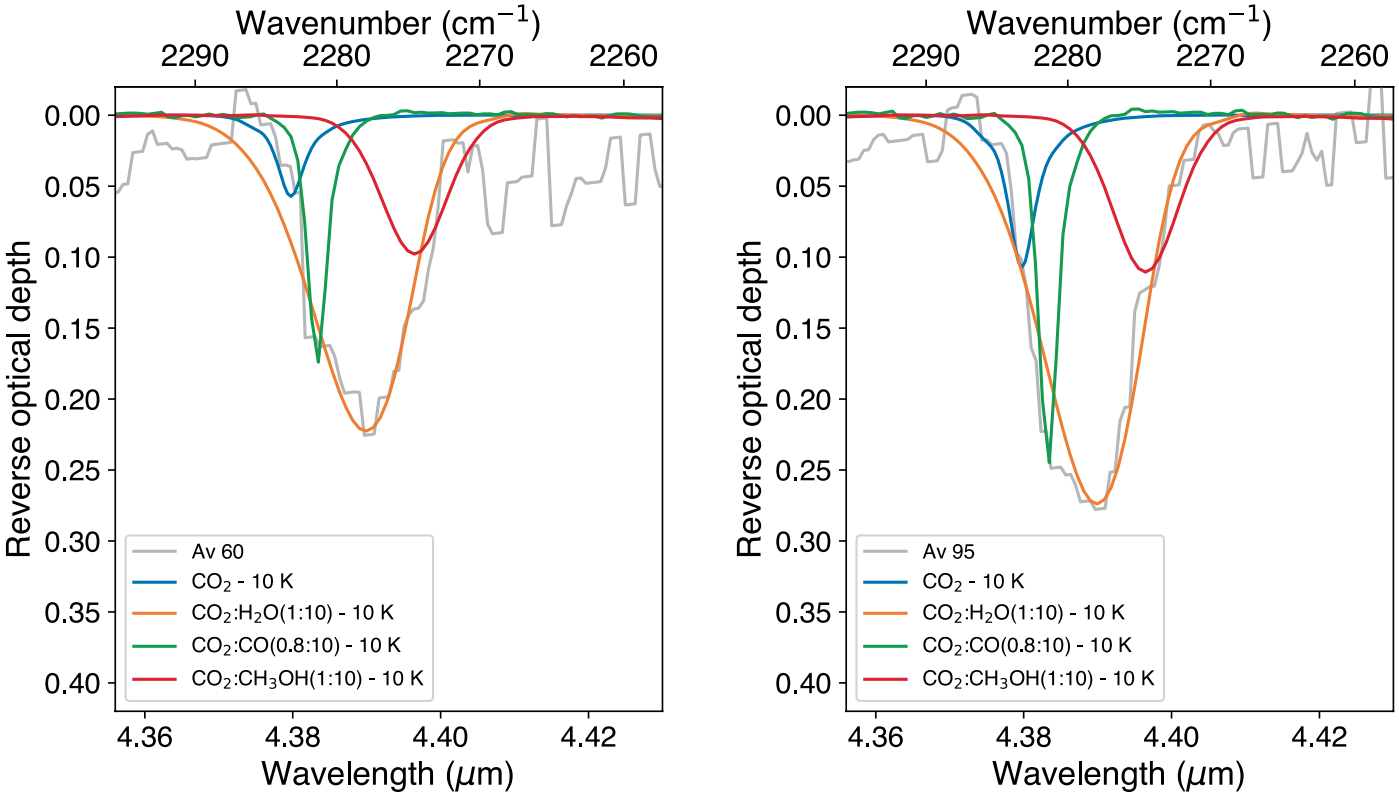

Extended Data Fig. 4 | Observed absorption profile of the $^{13}CO_2$ asymmetric stretching, around 4.39 μm, in NIR38 (left panel) and J110621 (right panel). To demonstrate the ice chemical environment that best reproduces the observed feature peak, the coloured curves show the scaled profiles of $^{13}CO_2$ in laboratory spectra of the following ice mixtures at 10 K: pure CO_2 (blue), H_2O:CO_2 (orange), CO_2:CO (green), and CO_2:CH_3OH (red). In all the ice mixtures, CO_2 is diluted in a ratio of ~1:10, with $^{12}CO_2/^{13}CO_2$ ~ 90.

https://doi.org/10.1038/s41550-022-01875-w

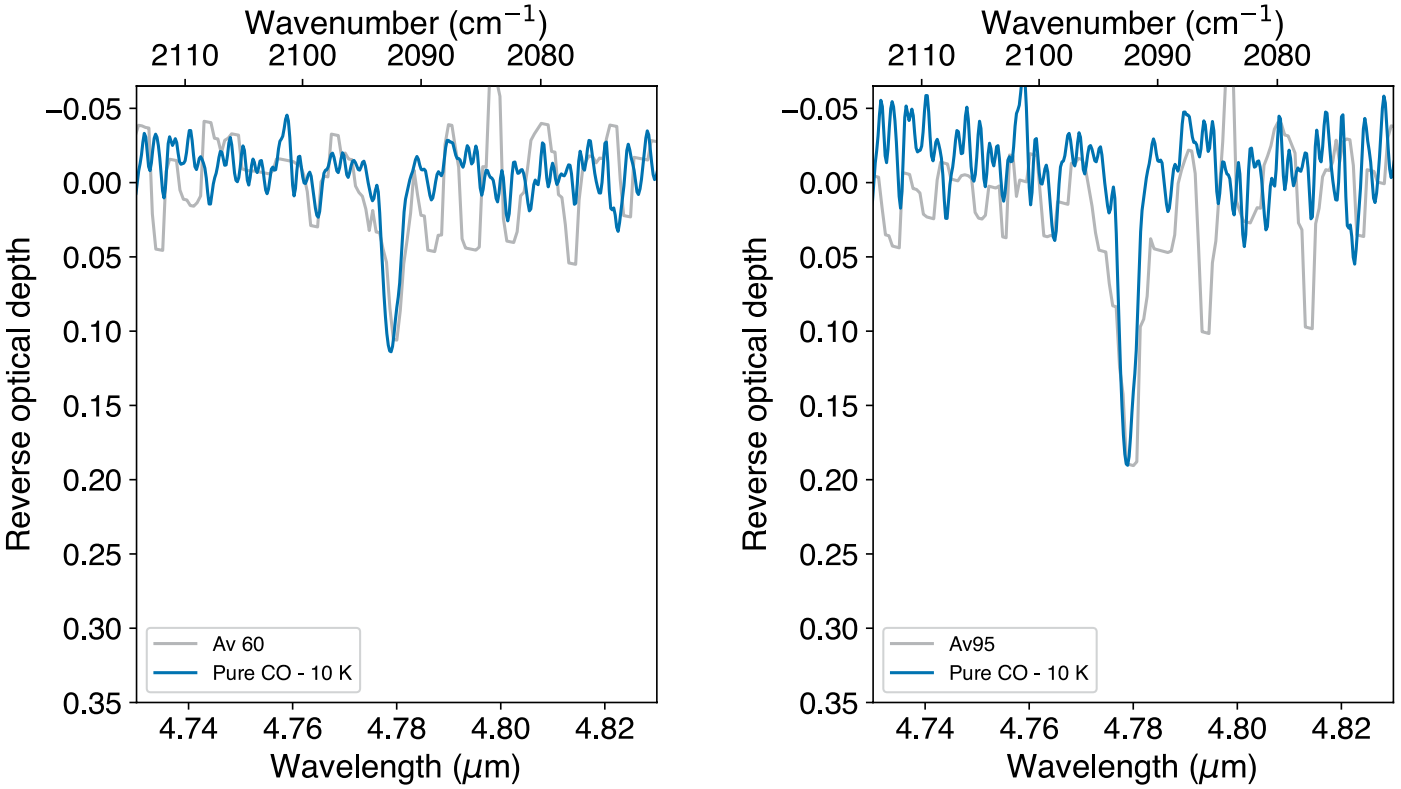

Extended Data Fig. 5 | Observed absorption profile of the ^{13}CO stretching, around 4.78 μm, towards NIR38 (left panel) and J110621 (right panel). The laboratory spectra of pure ^{13}CO ice at 10 K are also shown in blue.

https://doi.org/10.1038/s41550-022-01875-w

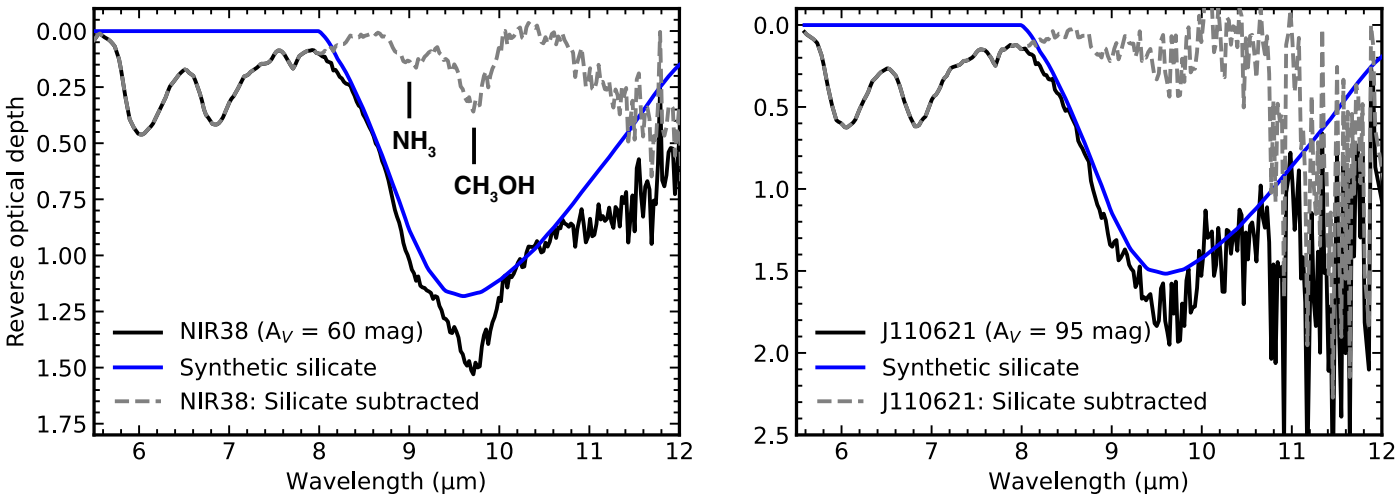

Extended Data Fig. 6 | Silicate subtraction during optical depth calculation for NIR38 and J110621. MIRI/LRS spectrum of the two background stars before (black) and after (blue) silicate subtraction. The grey dashed line is the synthetic silicate spectrum used to remove the silicate absorption toward the background stars.

https://doi.org/10.1038/s41550-022-01875-w

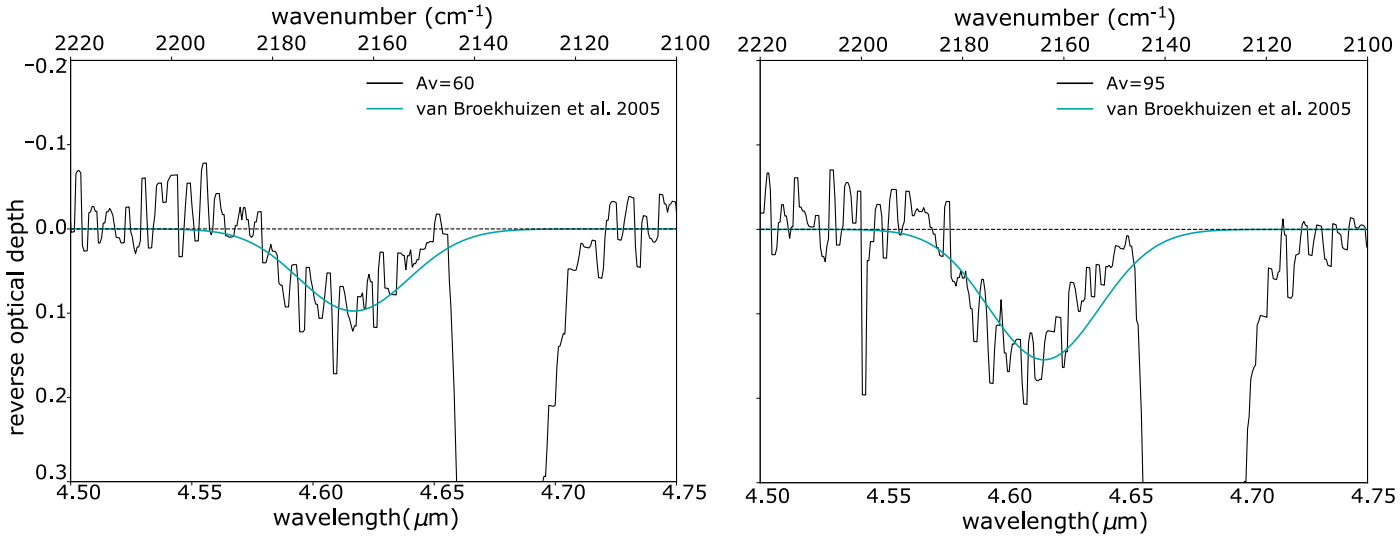

Extended Data Fig. 7 | Observed absorption profile of the OCN^- feature around 4.62 μm, towards NIR38 (left panel) and J110621 (right panel). A Gaussian fit using the parameters found in the literature[62] is also shown.

https://doi.org/10.1038/s41550-022-01875-w

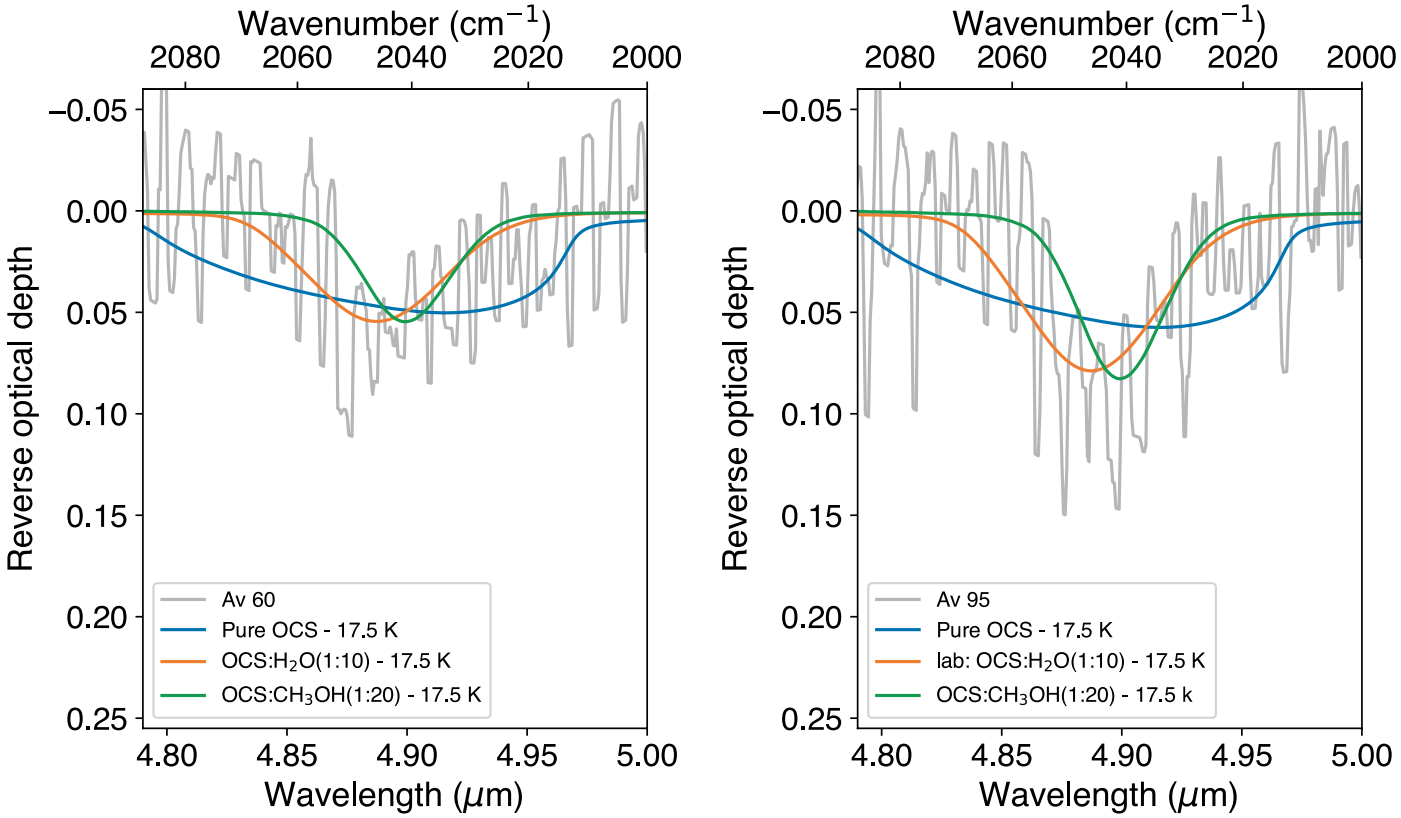

Extended Data Fig. 8 | Observed absorption profile of the C=O stretching of OCS, around 4.9 μm, towards NIR38 (left panel) and J110621 (right panel). The coloured curves show the profile of the OCS in laboratory ice spectra of pure OCS(blue), H_2O:OCS (orange), and CH_3OH:OCS (green), all at 17.5 K.

https://doi.org/10.1038/s41550-022-01875-w

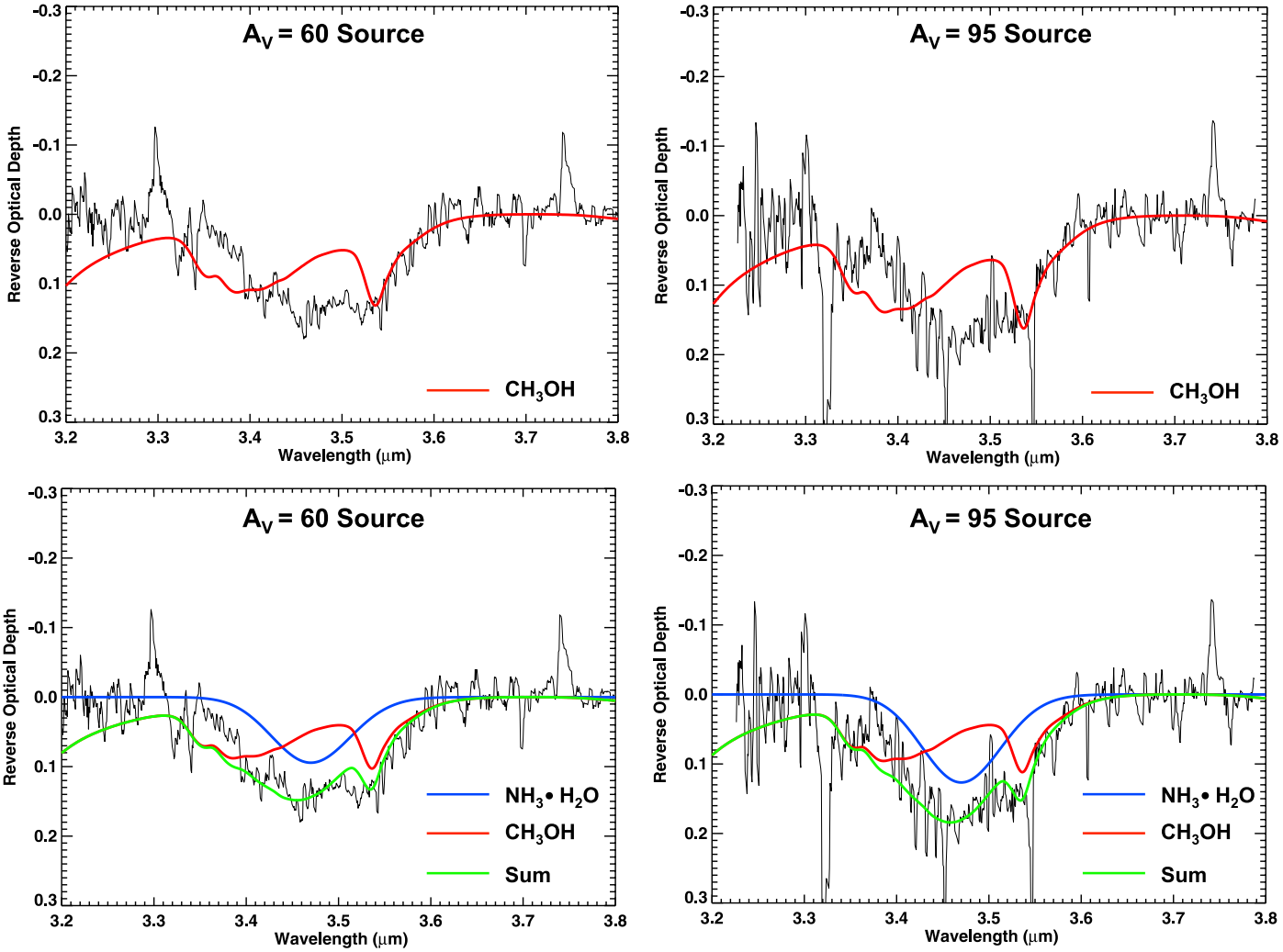

Extended Data Fig. 9 | Optical depths of the A*V* = 60 mag (NIR38, left) and A*V* = 95 mag (J110621, right) background sources in the 3.2–3.8 μm (3125 - 2631 cm^{-1}) region. Top: The red line shows the optical depths of CH_3OH laboratory data at 15K scaled for the C–H stretching band around the 3.53 μm feature. Bottom: The blue Gaussian represents the likely $NH_3 \cdot H_2O$ component centred at 3.47 μm and the red line again displays the CH_3OH laboratory data but both are simultaneously scaled so the sum (in green) fits the data from 3.40-3.65 μm.

https://doi.org/10.1038/s41550-022-01875-w

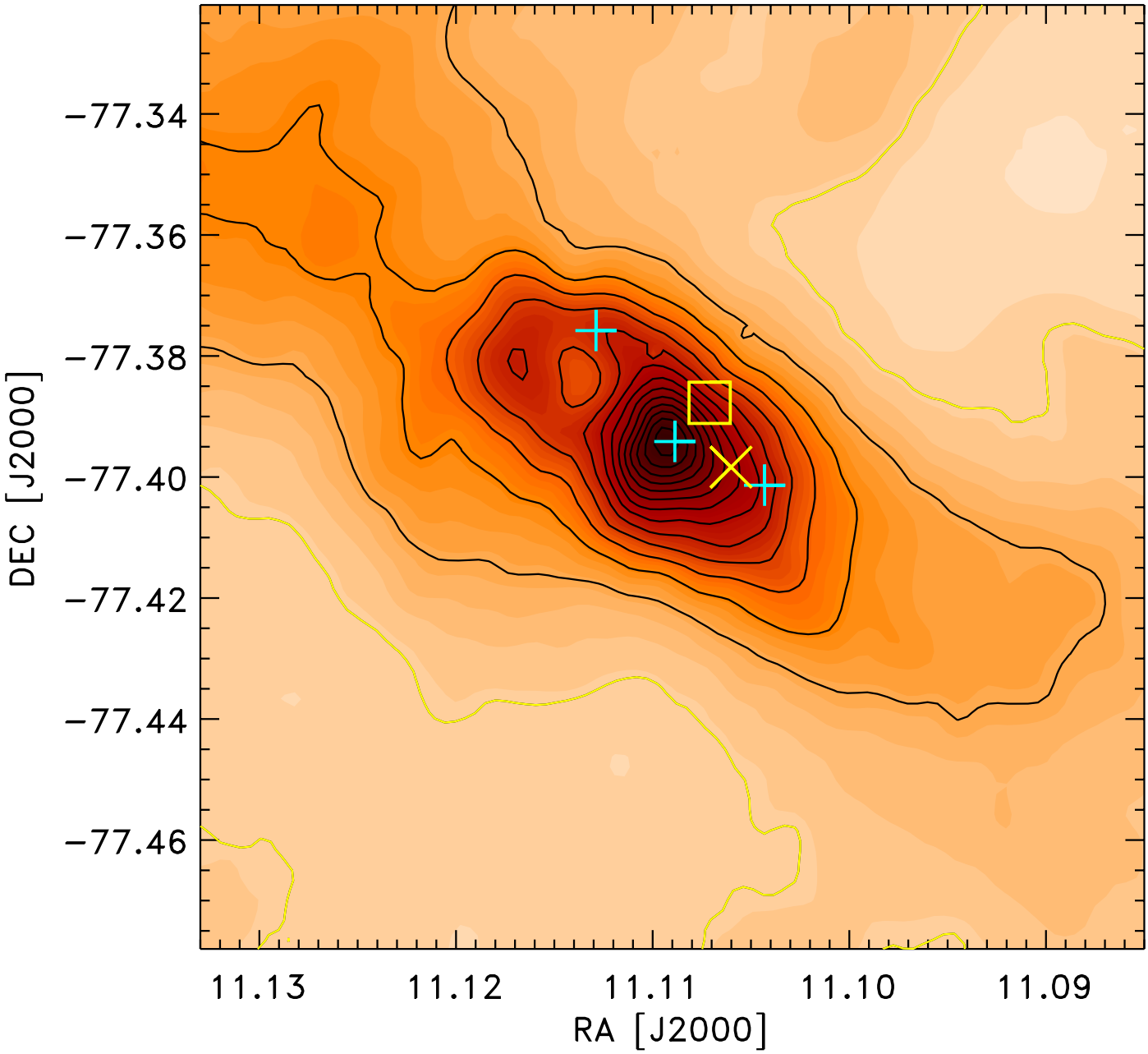

Extended Data Fig. 10 | Map of the column density distribution in the region inferred from the Herschel far-infrared maps from 70 to 500 μm. The cyan plus-signs indicate the locations of the Class I protostar Ced 110-IRS4, the Class 0 protostar ChamI-MMS and the clump Cha1-C2 going from the north-east (top-left) to south-west (bottom-right). The yellow box and cross indicate the location of the background stars NIR38 ($A_V \approx 60$ mag) and J110621 ($A_V \approx 95$ mag), respectively. The contours indicate increasing H_2 column densities in steps of 5×10^{21} cm^{-2}, starting at a value of 5×10^{21} cm^{-2} for the lowest contour (yellow line).